UNIVERSITÉ DE GENÈVE

Département de Physique Nucléaire et Corpusculaire

FACULTÉ DES SCIENCES

Travail de Master

Particle identification analysis using data taken by a prototype scintillator-based timing detector at the CERN PS

Auteur: Rebecka SAX

Directeur de mémoire: Prof. Philippe MERMOD

Superviseur: Dr. Alexander Korzenev

23 Mai 2019

UNIVERSITÉ DE GENÈVE

Abstract

The general interest of this project is to characterize and study the timing techniques of a Time-of-Flight (ToF)-detector. Identifying which particles (PID) are in the beam and when they arrive onto plastic scintillator counters, whose readout system is based either on photo-multiplier detectors (PMTs) or silicon photomultiplier detectors (SiPMs), is a key aspect of the project. This is done by measuring the time of flight of the particle in question and linking it to the mass of this particle. Information about the exact astronomical time of the arrival at the target and m^2 is given to a fellow group working on SuperFGD[1] for the ND280-T2K[2] upgrade.

In order to acquire this information, an analysis of the amplitude versus the time of flight (more precisely, vs. the so-defined *predicted time delay*) for the PMT- and SiPM-detectors has been made. Corrections due the dependence of the time measurement of the signal amplitude (so called *time-walk* corrections) concerning the SiPM-detectors have been applied. A formula for the time of flight is derived to be able to reconstruct the masses squared of the particles in the beam from their time of flight. This allows for particle identification.

Lastly, the uncertainties in the timing measurement, mass squared and in the momentum of the particles in the beam are discussed and the highest contribution to m^2 identified.

NB. Natural units will be used in the discussions of beam momenta and particles masses throughout the investigation, if not noted otherwise. Lengths and times will be in SI units.

---

[1]Super fine grain detector.
[2]Near detector of T2K experiment in Japan.

Contents

1 Introduction

During the summer of 2018 data was acquired at the East Area (T9 and T10) at CERN PS[3] when a beam of particles (of momenta ranging from 0.3 GeV to 5.0 GeV) was shot through different compositions of magnets (quadrupole and sextupole) and detectors (Cherenkov, PMT and SiPM). The plastic scintillators which use PMT in the readout are noted S_1 and S_2 and the plastic scintillators using SiPM, S_3. Further in the text S_1 and S_2 are called 'PMT detector' and S_3, 'SiPM detector'. The Time-of-Flight (ToF)-detector includes only S_1, S_2 and S_3. The data from this detector has been analyzed in order to identify the particles composing the beam and arriving at the detectors. The particles that can be identified in this analysis are: electrons, muons, pions, protons and kaons.[4]

The ToF technology and setup at the East Area is suggested for the upgrade of the ND280-T2K in Japan and as a timing detector for the SHiP[5] experiment[6] at the CERN SPS[7]. The thesis is hence organized as following. The first sections 1.1 and 1.2 allow for a brief explanation of the physics goals and how the timing techniques are used in the two experiments. In section 2 the experimental setup is discussed, notably the beam (2.1), the magnets (2.2), the collimator (2.3), the Cherenkov detector (2.4), the PMTs (2.5), the SiPMs (2.6), the scintillators (2.7) and the data acquisition system (2.8).

Section 3 discusses the experimental approach. Each particle species will possess a specific time of flight (Δt), which represents the time it takes for it to go from one detector to another. Hence a cloud of points (representing the particles arriving on the detector) will be observed around these specific Δt. Each cloud should correspond to a certain particle species. In order to know what cloud of points would correspond to what particle species, a formula that links the time, distance and momentum to the mass will be introduced. With the help of the reconstructed mass the exact particle species can therefore be identified (sections section 3.1 and 3.1). The predicted time delay will also be introduced and explained (3.2) as well as the treatment of uncertainties (3.3).

The analysis procedure (section 4) is organized in the following way. Firstly, the particles, with a given momentum arriving on the detectors, will be represented as points on a graph of the amplitude (in volts) as a function of the predicted time delay (in ns), see section 4.1. They will be plotted using data from the PMT- and SiPM-detectors, the two counters being the same type of detector in the sense that they acquire the exact same data. Their main difference (setup-wise for the experiment) is their position along the beam line (see section 2). However, their analysis will not be done in the exact same way as the SiPM-detectors will have to be corrected for an effect called *time-walk* (section 4.2). The mass squared of each particle will then be identified (section 4.3) and lastly the uncertainties in time and mass squared will be analyzed (sections 5.1 and 5.2). This will allow the uncertainty in momentum to be identified as well as the greatest contribution (momentum spread or timing measurement) to the uncertainty in the mass squared.

Based on the discussion of section 4 and 5 an evaluation will be made, which will form a summary (section 6) and conclusion (section 7).

---

[3]Proton Synchrotron

[4]Kaons will be produced given a high enough energy since they undergo pair production, to conserve strangeness and $E^2 = p^2 + m_0^2$.

[5]Search for Hidden Particles

[6]To be approved for construction.

[7]Super Proton Synchrotron

1.1 Timing detection and physics goal of ND280-T2K upgrade

The T2K experiment is a long baseline neutrino oscillation experiment situated between Tokai (on the east coast of Japan) and Kamioka (295 km west). In Tokai, a facility called J-PARC accelerates protons (up to 50 GeV), which collide with a graphite target to produce pions. The pions will decay into muons and muon neutrinos. A muon-neutrino beam is obtained by placing a second layer of graphite which will stop the protons and muons but let the neutrinos pass through.

Once penetrated the second graphite layer, the $\nu_\mu-$beam will first pass through the Near Detector (ND280) situated 280m from the graphite target. ND280 will acquire useful data of the beam before the neutrino oscillations occur such as (most importantly) the number of muon neutrinos constituting it. Secondly, the $\nu_\mu-$beam will travel 295 km to the Super Kamiokande detector[8] where it enters a very large cylinder of ultra-pure water (50000 tons). Thanks to the high energies of the neutrinos contained in the beam, a few of them will interact with the water. The interactions involving ν_μ will produce muons and the ν_e interactions, electrons. If they have velocities higher than the speed of light in water, the produced muons and electrons will, as they pass, give rise to a cone of light of Cherenkov radiation. Sensitive photo-multipliers which are placed on the walls of Super Kamiokande will detect such radiation in the form of a a ring and will be able to distinguish muons (sharp ring) from electrons (diffuse ring).

The physics goal of T2K is to investigate the oscillations of neutrinos and namely to deduce the difference between the squares of the masses of the neutrinos and the mixing angle θ_{ij} where, $i \in \{1,2\}$ and $j = 3$ [1]. It was the first experiment to ever observe oscillations of muon neutrinos to electron neutrinos (June 2011).

The physics goals of the near detector of the T2K, ND280 is to measure:

- the flux and energy spectrum of the ν_μ beam

    - the goal of the ν_μ disappearance analysis is to measure θ_{23} and Δm_{23}^2

- the ν_e-content of the beam and its energy spectrum

    - the goal of the ν_e appearance analysis is to measure θ_{13}

Additionally to these measurements, the ND280 performs accurate measurements of various neutrino interactions which either contribute to the backgrounds in the appearance and disappearance studies or are needed for the sterile-neutrino analysis.

The proposed ToF-detector for the ND280-T2K upgrade is shown below in figure 1.

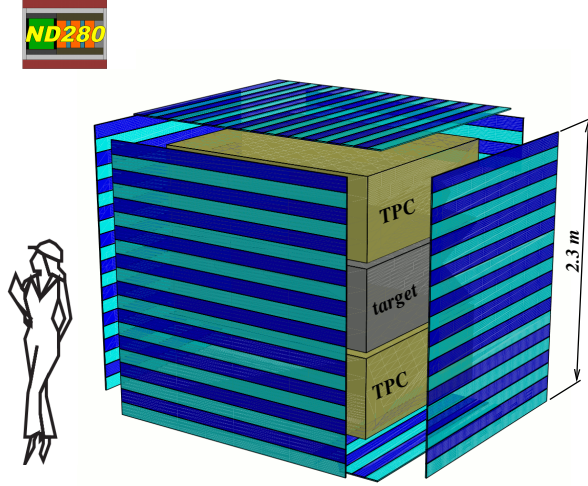---

[8]Also called the Far Detector.

Figure 1: Schematic view of the proposed timing detector of the ND280-T2K upgrade [**2, 3**].

The grey rectangular cuboid is the active target volume on which TPCs[9] are placed above and below. The plastic scintillators (the detector planes) surround the three cuboids on all exposed faces. The whole system is located inside a region of high magnetic field (0.2 T). This, and the fact that the ND280-detector is very compact (hence limited space) encourages the use of the SiPM detectors (see section 2.6 on the pros and cons of SiPMs vs. PMTs).

The current idea[10] is to assemble a total of 118 bars around the detector. They have a length of $2.0 - 2.3$ m, which provides a time resolution of 140 ps along the bar. The SiPMs, in an array of 8 per ASIC, will be placed on both ends of each bar. The total number of SiPMs is therefore 1888 and the total number of DAQ[11] channels is 236.

The detector itself seeks to determine the trajectory direction of particles, produced from neutrino interactions. Identification is also possible from this configuration since the particles will have energies around the 100 MeV-region (the peak energy of the neutrino beam being 0.6 GeV).

1.2   Timing detection and physics goal of SHiP

The SHiP experiment is a yet-to-be-approved experiment that would be installed at CERN, SPS [**4**]. Currently technical proposals of the experiment have been submitted and analyzed in the hope of its approval. The physics goal of the experiment is to Search for Hidden Particles (hence SHiP). More specifically, SHiP will be able to observe (if they exist) Heavy Neutral Leptons (HNLs), which are very weakly interacting long lived particles. Other yet-to-be-confirmed particles such as light supersymmetric particles (sgoldstinos) could also be observed in this detector. The setup also allows for a thorough study of tau neutrinos.

The proposed timing detector of the SHiP experiment is shown below in figure 2.

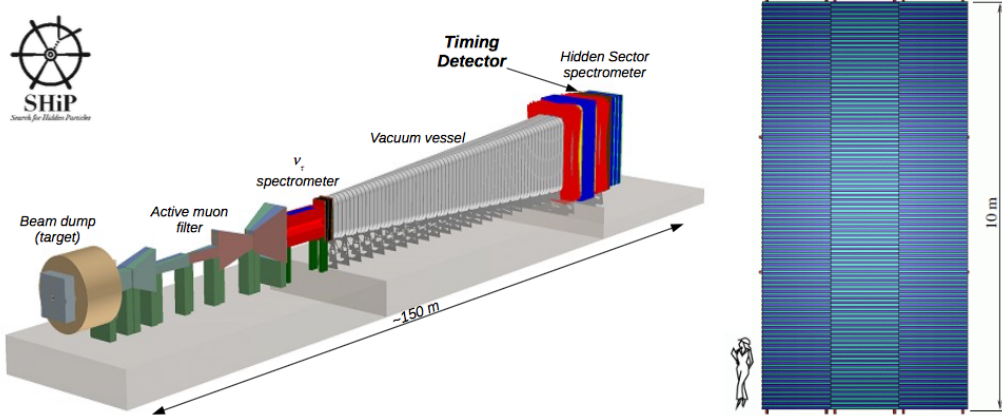[9]Time Projection Chamber
[10]November 2018
[11]Data acquisition

Figure 2: Schematic view of the proposed timing detector of SHiP [2].

The detector will cover a 5×10 m^2 area and will be positioned downstream the vacuum decay vessel. Its purpose is to reduce combinatorial background[12] by matching the times of arrival of particles belonging to a single event. It will also be able to identify particles with a momentum of a few GeV thanks to the required time resolution which is under 100 ps. The timing resolution limits the bar length to about 2 m. From its coverage area it can be deduced that an array of 3 columns and 182 rows with 1.67 m long bars will be used. This is the present[13] design of the detector, thus giving a total of 546 bars, 1092 channels and 8736 SiPMs.

---

[12]Vertices made by a random muon crossings.
[13]November 2018

2 Experimental Setup

In this section the experimental setup for the test-beam measurements at the CERN PS will be discussed in detail - notably, the composition of the secondary beam and how it was produced, what type of magnets were used and how the collimator works. The question of why certain detectors were chosen and why they where placed at specific locations will be answered. Their functioning will also be addressed as well as the acquisition of the data.

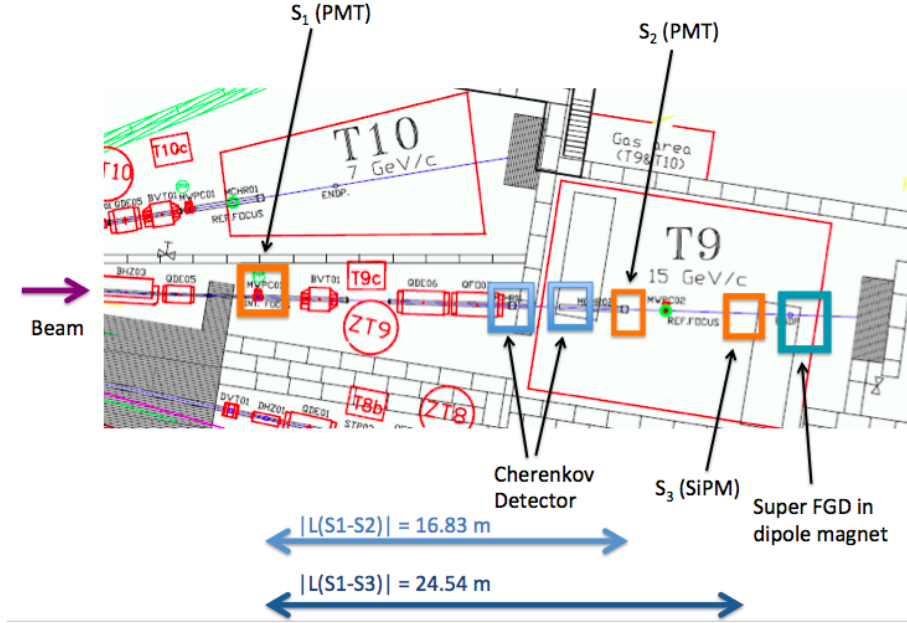A sketch of the experimental setup is shown below in Figure 3.

Figure 3: A top view of the experimental setup at T9 of the East Area of CERN PS [5].

The beam passes through quadrupole and dipole magnets (the red rectangular boxes along the beam line), the PMT and SiPM detectors as well as two Cherenkov detectors. Lastly it arrives at the Super FGD detector, which is located inside a dipole magnet.

The location of the PMTs and SiPMs are noted by S_i ($i = 1, 2, 3$), where the S stands for scintillator. The distance from S_1 to S_2 or to S_3, respectively is noted by $L(S_1 - S_2)$ and $L(S_1 - S_3)$. Their exact values are are shown in Figure 3. The trigger in the test beam was formed by the coincidence between signals of all three counters. S_1 is taken as a first chronometer (a *start* button if one prefers). The second chronometer (the *stop* button) is either S_2 or S_3, depending on what data is desired to be analyzed (i.e. PMT or SiPM).

It is important to note that the principles of running of the detectors are *per se* the same as they detect the same type of events. That is to say, they give off the same type of data with only a difference in the time of flight. When analyzing the technology of light conversion to electronic signal of S_1/S_2 and S_3, one realizes that they are very different and possess both advantages and disadvantages (see section 2.6). The exact reason for the placement of S_1, S_2 and S_3 is to have an order of 10 m of separation which is required in order to perform PID of a beam in the order of: $0.1 - 10.0$ GeV.

2.1 The beam

The beam passing through T9 and T10 of the East Area at the CERN PS is a secondary one. The primary beam comes from the PS, which accelerates protons up to 24 GeV. When this beam hits an aluminum[14] production target new hadrons are created which will form the secondary beam [6]. The interest of using a secondary beam as opposed to using a primary one is to have a beam of lower momentum particles of various species (which is needed for a ToF and Super FGD study). In order to experimentally obtain the exact momentum desired for the study a careful choice of the value of the magnetic field[15] of the dipole and quadrupole magnets is made. The momentum of the secondary beam, the beam used in this ToF study, will be of fixed value between $0.3 - 5.0$ GeV. However, there will be an uncertainty related to this momentum. In section 3.3 its extraction is explained and in sections 5.1 and 5.2 its importance deduced.

The exact composition of the beam depends on its momentum and the sign of the charge of the beam particles (positive or negative). More specifically, a negative beam contains anti-protons, K^-, π^-, μ^- (After the decay of π^-) and electrons and a positive beam is a composition of protons, K^+, π^+, μ^+ (After the decay of π^+) and positrons. Be that as may, the goal of our study is to identify the masses of our particles and since $m_p = m_{\bar{p}}$ the sign of the beam is not of strict relevance. The results obtained with a positive and negative beam for a given momentum will also be compared (see section 4.3.4).

The fraction of different particles composing the T9 beam as a function of its momentum is shown below in Figure 4, for both positive and negative beams. They are Monte Carlo simulations (courtesy of the PS team) of the beam just after the production target.
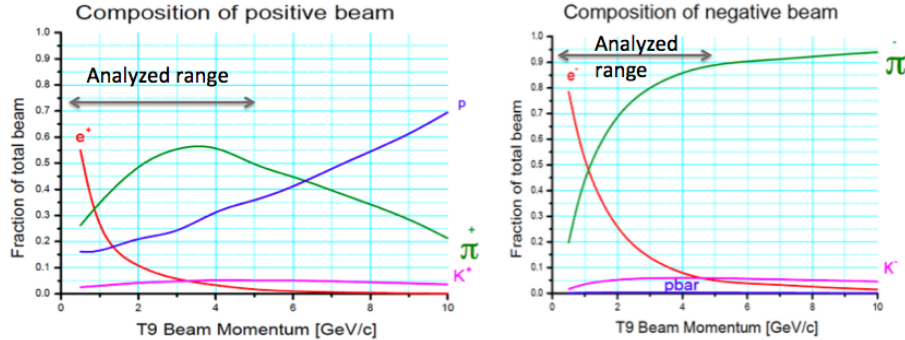

Figure 4: The T9 beam composition at the East Area of CERN PS [5].

Figure 4 shows that is that there is a higher fraction of electrons that forms the negative beam than that of positrons in the positive beam at low momenta. Concerning the pions, π^+ hits a peak fraction of total beam at around 3 GeV however π^- continues to increase after this value, towards higher momenta. This is due to the fact that there are a fewer amount of anti-protons in the negative beam as compared to protons in the positive beam where the amount of the latter increases with an increase of momentum. One can in general conclude that there are very few anti-protons (confirming that we live in a matter-world and not an anti-matter one). Finally we see that more or less the same amount of kaons (+ or −) composes the positive, respectively the negative beam. A final remark to make is that no muons are plotted on the these graphs as they are plotted from simulations just after the production target. This means that no muons are yet detected. They are produced as a result of the decay of the pions, which haven't had time to yet decay. The range of analysis is noted on Figure 4.

---

[14]Length: 200 mm and diameter 10 mm.
[15]We actually set the current, using a program called CESAR, which will in turn change the magnetic field.

One should always in such type of experiments take into account the background and how to suppress it, in order to have as pure results as possible. In complete generality, background (in this case) is particles that happen to be in the beam but did not come initially from the target production interaction. For example, particles created from interactions of the beam with the elements of the beamline or with the surrounding air. Background can also be particles that are created as a result of decay of the initial particles produced in the target interaction. Their momenta will be very different with respect to the nominal one, which makes it impossible to attribute them to a certain mass peak. All these types of background will contribute to our study. An example of the latter is the detected muons, where most of them are produced in the decay of the pions in the beam. However in this case, a specific mass peak can be attributed to the muons since in the decay of pion (not at rest) into muon almost all energy is given to the muon and very little energy is absorbed by the produced neutrino.

2.2 The magnets

Around the beam path magnets are placed in order to guide the beam and control its size. The dipole magnets bend the particle trajectories in a given direction. The specific direction depends on the sign of the charge of the particles. The "strength" of the bending is a function of the magnetic strength of the dipole.

The size of the beam spot and so also the position of the focus of the particles in it is adjusted through the help of quadrupole magnets who will focus the beam in one plane which automatically defocusses in the other plane. A game of focussing and defocussing will thus take place until the goal, to have a beam as focussed as possible, is reached. For this to happen it can be that sextupole magnets are added along the beam line[16].

2.3 The collimator

To collimate means 'to bring into line' or 'to make parallel' hence the goal of the collimator, to do precisely this to the beam. It has a more fundamental job than the quadrupole or sextupole magnets as, for the case of the horizontal collimator, it will directly reject particles having a trajectory that is too far away (as compared to a predetermined range), thus minimizing the spread of momenta of the beam. The vertical collimator will reject particles that leave the target at angles larger than a predetermined range in order to, once again, bring the beam into line. Our beam is at 0° to the horizontal.

2.4 Cherenkov detector

A Cherenkov detector will detect Cherenkov radiation which is produced by particles travelling in a medium at a speed higher than that of light in that medium. The medium is a gas whose pressure one can adjust so as to choose what particles would emit such light, as a specific pressure would imply a specific velocity threshold which, if particles possess this minimum, would give out radiation. The velocity can then be translated into a mass (as momentum is assumed to be fixed) thence one can discriminate between particles.

The setup uses CO_2 as the gas, at atmospheric pressure (1 bar). The particle type which will be identified with this detector and these specific settings can be better understood by analyzing the following graph:

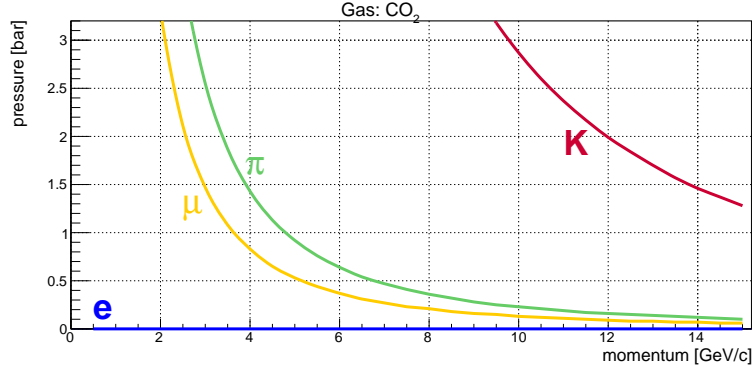[16]This is a general statement, our beamline has no sextupole magnets.

Figure 5: Pressure vs. momentum for which particles emit Cherenkov radiation.

The x-axis corresponds to the momentum in GeV/c and the y-axis represents the pressure in bar. The lines show the threshold, i.e. the minimum value of momentum at which the particle in question will emit Cherenkov light. For example, at a pressure of 1.5 bar muons will emit Cherenkov light at a momentum of 3 GeV/c and above. As can be seen electrons have a very low threshold (they are ultra-relativistic even at low momenta). Muons being next followed by pions and finally kaons. Protons are even further away at very high momenta, thus not even fitting on the graph. For the range of momentum of $0.3 - 1.0$ GeV/c (remembering that the pressure in our beamline is of 1 bar), electrons (and positrons) will be the only particles emitting this type of radiation. For the beam of 5.0 GeV/c, muons and pions will also emit Cherenkov photons.

2.5 Photomultiplier detectors (PMTs)

The beam first passes S_1 then comes to S_2. Both counters use PMTs to detect photons produced in the scintillator. The PMTs give knowledge of the time of arrival of the particles at S_1 and S_2 (denoted in the following by: t_1 and t_2). One can hence deduce the difference in time of arrival at S_1 and S_2, $|t_1 - t_2|$ which is the time of flight of the particles. The processes from the arrival of the photon onto the PMT and into an electrical signal, will be explained in the following.

The purpose of a PMT is to convert photons into an electric signal. More specifically, when a photon (with energy ranging from near infra-red to ultraviolet) enters a PMT, i.e. a vacuum bulb, it will hit a photocathode plate, which will, via photoelectric effect, eject an electron. Firstly, the emitted electron will pass a focussing electrode, who's purpose is to regulate its outgoing direction. Secondly, thanks to a potential difference the electron will be accelerated to the first dynode. Because of the increase in its kinetic energy, a few electrons will be ejected from this dynode. They will in turn be accelerated to the second dynode where even more electrons will be ejected and so it will go on through the twelve dynodes. The potential will increase when traversing the dynodes (from the first to the last), the potential difference being about 100 V between them. Finally, a detectable current (composed of all these electrons) will be obtained from the single photon. A sketch of a PMT is shown in figure 6.
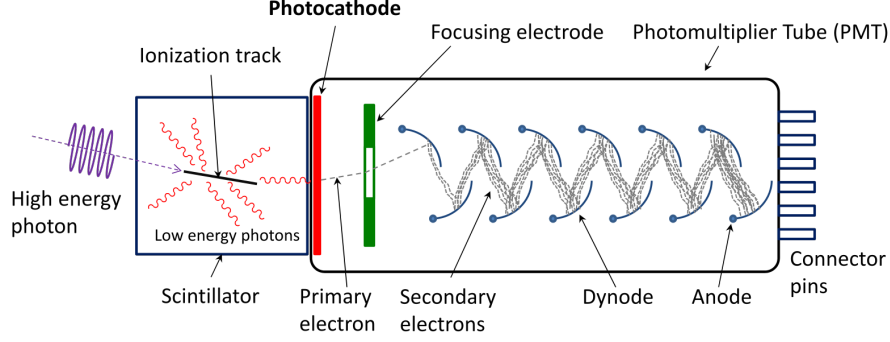
Figure 6: Sketch of a photomultiplier tube coupled to a scintillator [7].

Below are photos of the beam counters, with PMT readout, their plastic scintillators and cables, along the beam line, for S_1 and S_2.

(a) Beam counter S_1.
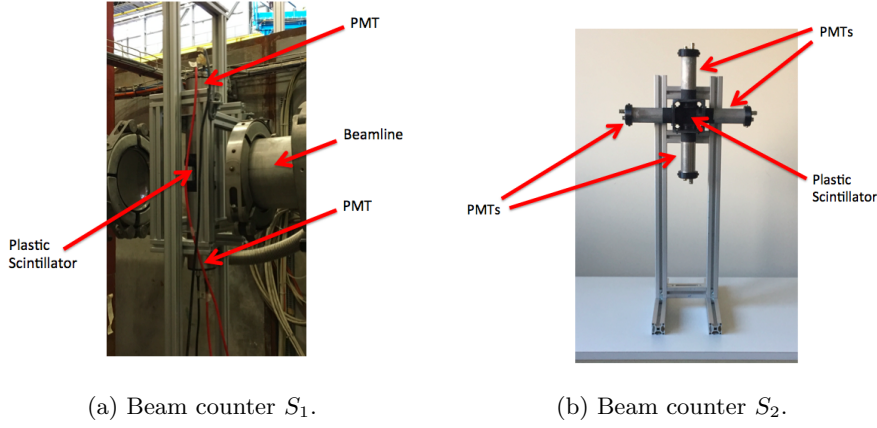

(b) Beam counter S_2.

Figure 7: Beam counters using PMTs for readout.

Figure 7a has one PMT placed on top pointing downwards and another one below pointing upwards. In between them there is a plastic scintillator (EJ-228, $4 \times 4 \times 0.5$ cm^3). One can also observe the beam line in which the beam passes.

Figure 7b is taken from before the beamline installation. S_2 takes the shape of a cross, formed by four PMTs, whereas S_1, consists of only two PMTs. Since the PMTs are smaller here (a question of cost), a cross is used. This allows the available area of detection to be the same as for S_1. The same plastic scintillator as for S_1 is used.

2.6   Silicon photomultiplier detectors (SiPMs)

The detector located at S_3 uses a silicon photomultiplier for light registration, which is a solid-state silicon detector with single photon counting capability, based on a single-photon avalanche diode (SPAD). A SPAD is a solid-state photodetector which, thanks to a photon-generated carrier and the internal photoelectric effect, can trigger a relatively large (though short-duration) avalanche current. A mechanism called impact ionization, where electrons (and/or holes, i.e. carriers) are accelerated to high kinetic energies through a large potential gradient (voltage), will create this avalanche. Depending on the kinetic energy of the carriers, i.e. if it is large enough, further carriers

will be liberated from the atomic lattice. The kinetic energy available is a function of the ionization energy of the bulk material. Therefore an exponential increase in the number of carriers will take place and so create a signal.

There are many advantages of SiPM detectors over classical PMT detectors (see section 2.6). They can for example be coupled directly to a scintillator bulk and so yield a timing resolution of sub 100 ps. In this project, arrays of 8 SiPMs, manufactured by Hamamatsu, model S13360-6050PE are used. An image of an array of 8 SiPMs is shown below:
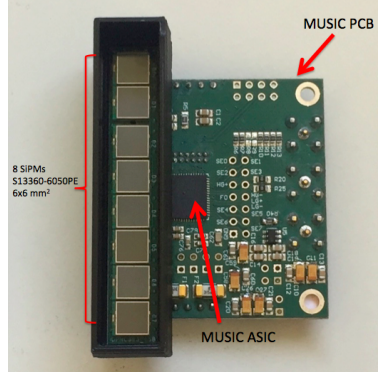

Figure 8: Array of 8 SiPMs 6×6 mm^2 with MUSIC chip mounted on PCB, used for readout of S_3 counter [2].

The 8 SiPMs can be seen on the left of the chip. The PCB is the green board and the MUSIC chip is the black square. These are placed on the edges of the scintillator bar.

Advantages of SiPM vs. PMT

The SiPM detector has a size of about 6×6 mm^2, which hence leads to the *compactness* of the detector. Whereas classical PMT detectors would need more space (cylindrical with length of $\approx$ 30 cm and diameter of $\approx$ 5 cm). Since the sensors are coupled directly to a scintillator bulk, the SiPM array can *take the form* of the bar cross-section. Thus no special adiabatic light-guides with complex shapes are needed. SiPMs also have the advantage of having a *low bias voltage* and being *insensitive to magnetic fields*, allowing it thus to be used in a magnetic environment, while PMTs require a ferromagnetic housing, rendering the construction bulky. Further, they possess a high photon detection efficiency 40% as compared to the PMT's 25% [2, 8]. Also they have a larger sensitive area $\sim$ 50 cm long bar of about 3 cm of width, hence being able to capture more photons than the PMT (sensitive area of 4×4 cm^2). An important remark to make is that the more photons detected, the better the timing resolution ($\sigma_t \propto 1/\sqrt{N_{p.e.}}$) [9], hence the interest of the SiPMs as timing detector.

Disadvantages of SiPM vs. PMT

SiPMs have a large capacitance which increases the rise time and width of the signal and thus worsens the time resolution. This problem is solved by using an independent sensor readout to isolate the sensor capacitances from each other. They also have a typical noise of about 50 kHz/mm^2, which is by several orders of magnitude higher than the noise of PMT. However, the threshold is not a problem for plastic scintillators with $2 \cdot 10^4 \gamma$ emitted per cm [2, 8].

2.7 Scintillators

The PMTs and SiPMs are coupled to a plastic scintillator, through which the particle will pass. A scintillator will, when struck by an incident particle, scintillate i.e. re-emit absorbed energy in the form of light. More specifically in this case, free electrons will excite from the kinetic energy of the incoming particle (for example electron, positron, muon, pion or proton) and then re-emit a photon. The scintillator will also act as a light guide allowing for conversion of the energy of the emitted photon to an energy in the visible/ultraviolet interval, which is the range of detection of the photomultiplier tubes.

The scintillators used are made of plastic, manufactured by Eljen Technology, more specifically the plastic: EJ-200 (for SiPM) and EJ-228 (for PMT). We show a table below of their properties.

	Wavelength of maximum emission [nm]	Rise time [ns]	Decay time [ns]	Attenuation length [cm]	Counter
EJ-200	425	0.9	2.1	380	S_3
EJ-228	391	0.5	1.4	< 10	S_1, S_2

Table 1: Table of properties of plastic scintillators used in the beam counters [10].

The wavelength corresponding to the maximum emission is the wavelength at which the highest number of photons would be emitted. The plastics used have $\lambda_{max} \approx 390 - 430$ nm, corresponding hence to the the range of detection of the PMTs. It is linked to the rise time of the scintillator from: $E = \hbar f = \hbar \frac{c}{\lambda}$, thus short wavelength implies a high energy. Using Heisenberg's uncertainty principle: $\Delta E \Delta t \sim \hbar$, a high energy implies a short emission time. Hence a shorter λ_{max} implies a shorter rise time. One should note that this is a very general conclusion and that in practice the energy loss is more complicated.

The rise time of a scintillator detector indicates the average time duration required by a scintillator to emit a photon. Respectively the decay time of a scintillator detector indicates the time it takes to go from a high photon yield to a low photon yield. In general one would wish for a short rise time to allow for a fast response. The emission time probability is given by $P(t) = \frac{e^{-t/\tau_{decay}} - e^{-t/\tau_{rise}}}{\tau_{decay} + \tau_{rise}}$, where the decay and rise times of each element are used. Below $P(t)$ is represented in a graph:
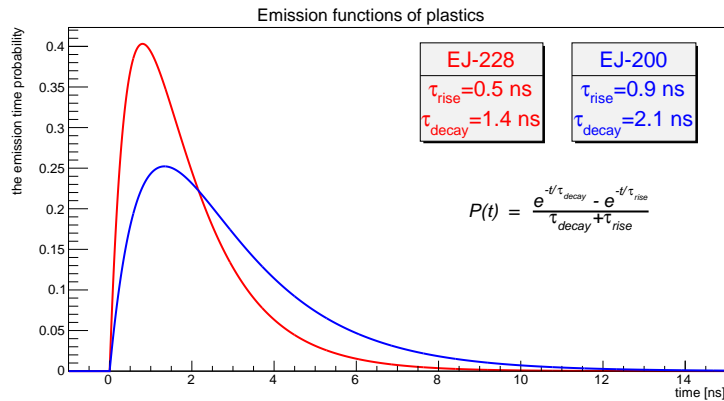

Figure 9: Emission time probability vs. time for the two plastic scintillators.

14

The function of the emission time probability, $P(t)$, is shown on the graph, where the values of τ_{rise} and τ_{decay} are defined for both plastic scintillators. $P(t)$ is plotted as a function of time.

The attenuation length of the scintillator is defined as the length for which the probability that a photon is not absorbed is $1/e$. This can come from lateral surface leak and reabsorbing. A short attenuation length implies a short rise time (and vice versa). The SiPMs are connected on the edges of a long scintillator bar (~ 50 cm) and so a longer attenuation length is needed. Hence a compromise between the two has to be made, and therefore the use of EJ-200 for S_3.

The spectral dependency, the attenuation length and the photon detection efficiency of a plastic scintillator will depend on the wavelength of the photons in question. The figure below links these quantities for EJ-200:
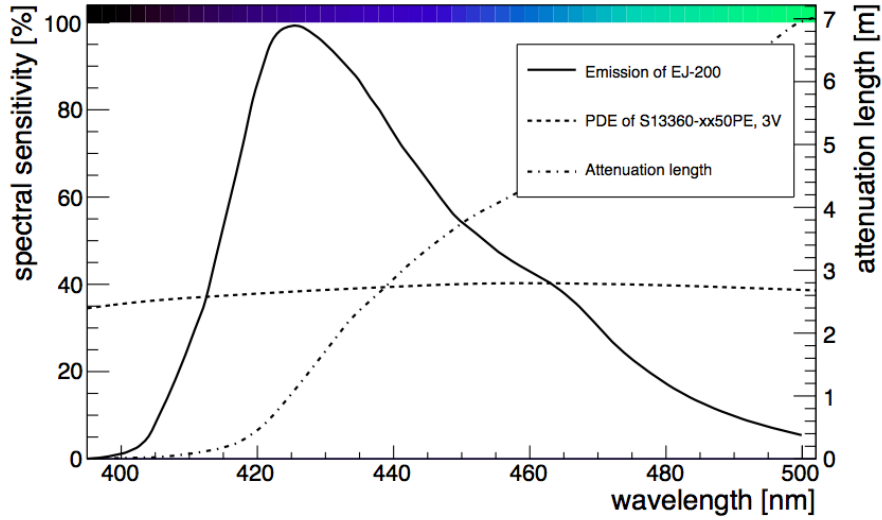

Figure 10: Emission spectrum and photo-detection efficiency of typical SiPMs and attenuation length as a function of light wavelength for the EJ-200 plastic scintillator [3].

Figure 10 shows that the emission spectrum resides in the near-UV region of the visible spectrum. At longer wavelengths, near the green, a better photon yield in long bars can be achieved as the SiPM photon detection efficiency is high (higher than PMTs at the same wavelength). One observes as well an increase in the attenuation length. Again it is clear that EJ-200 is ideal for the SiPM detector at S_3 as it provides a high light output, suitable optical attenuation length and fast timing (see table 1). All this together gives rise to a good timing resolution for S_3.

2.8 Waveform analysis

The data is acquired using an electronic module called *WAVECATCHER* [11], which is based on a waveform digitizer ASICs, called SAMLONG SCA [12]. It uses a circular buffer, with 1024 capacitors which records and stores an analogue signal at very high rate. The sampling rate of the analogue signal was fixed at 3.2 GB/s, which is equivalent to every 312.5 ps. If there is a trigger decision on the sample, the information is sent and stored in the PC. Its timing accuracy is about 5 ps and is chosen because it has a better internal time resolution than that of a scintillator counter, which is around 40 ps (see section 3.3). It has a bandwidth of 500 MHz which is well suited for detection of very short pulses.

15

The data is sent to a PC via a USB2 connection at a rate of 480 Mbit/s and saved directly on disk with Windows used as acquisition software. Below a print-screen of the DAQ program during data taking is shown:
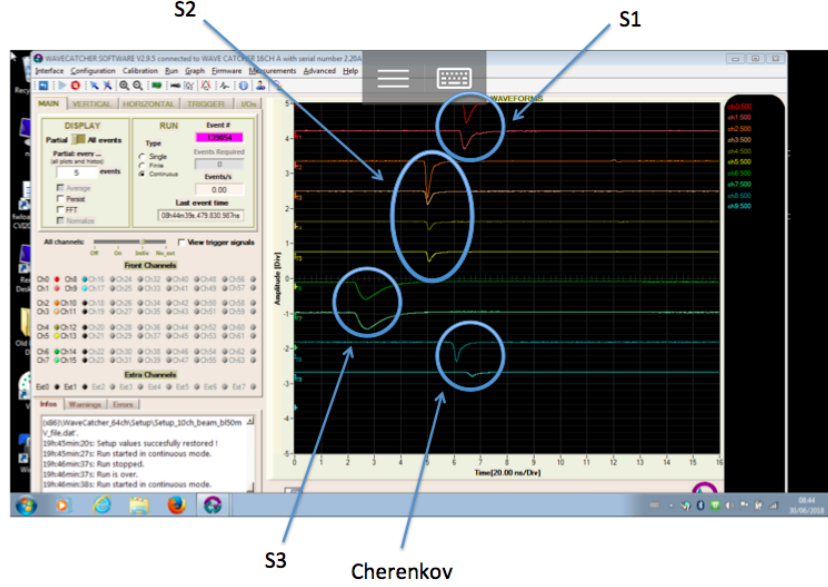

Figure 11: Screen-shot of the *WAVECATCHER* data acquisition program run under windows.

Figure 11 shows the amplitude of the signal as a function of time. The signals (the coloured curves) are represented as waveforms. One remarks that the signals arrive at different times. The signals from S_1 and Cherenkov arrive last, S_2 after that and S_3 first. This is due to the finite speed of the information passing through the cables and the difference in cable distance of the detectors to our DAQ module. As can be concluded from Figure 3, S_1 is furthest away from the DAQ module which is placed just before the Super FGD in the dipole magnet. S_1 will hence need longer cables and so it will take more time for signal to arrive to the DAQ module. S_3 is the closest and so the signal comes the fastest. Another remark to make is that there are several PMTs and SiPMs for each station, more specifically: two for S_1, four for S_2, two for S_3 and two for Cherenkov. The channels that are analyzed in the rest of the thesis are: Ch1 for S_1, Ch2 for S_2, Ch7 for S_3 and Ch8 for Cherenkov. Below one can see S_3 with the DAQ module.

Figure 12: Photo of S_3 counter in front of SuperFGD in the testbeam area of the CERN PS.

Figure 12 shows the end part of the experiment. One can note that the DAQ module and S_3 (the plastic scintillator bar) are close to each other, confirming thus the short cable length and so the fast signal. The low and bias voltage power supply are also marked out.

In the offline analysis the digital constant fraction discrimination (dCFD) technique was used for the analysis of waveforms. A dCFD takes time at a constant fraction of the peak height of the signal instead of a on a simple threshold value. This allows the detected time to be independent of the signal height, which is not the case for the fixed threshold method. The two methods can be understood from the graph below:
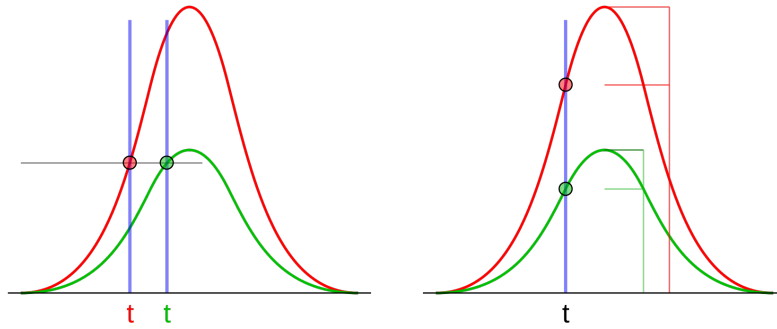

Figure 13: Fixed threshold (left) and constant fraction discrimination (right) [**13**].

To the left one has the fixed threshold triggering and to the right the constant fraction triggering. The first triggering method has to be corrected for the *time-walk* effect. In the analysis the SiPMs will need to be corrected due to *time-walk* (section 4.2). However this does not origin from the triggering method (as it uses dCFD and not fixed threshold), but from its electronics. The SiPMs use an ASIC called MUSIC that produces this effect.

17

MUSIC is an 8 channel ASIC for SiPM readout designed for high speed sampling (pulse between 5 and 10 ns). In order to create a short pulse, an attenuated and shorter signal is needed. This is done with a so-called *pole-zero cancellation*. It will reduce the peak duration of the signal and the tail produced by the sensor. The figure below (fig. 14) shows the response to a typical SiPM single cell pulse with and without the pole-zero cancellation [14].
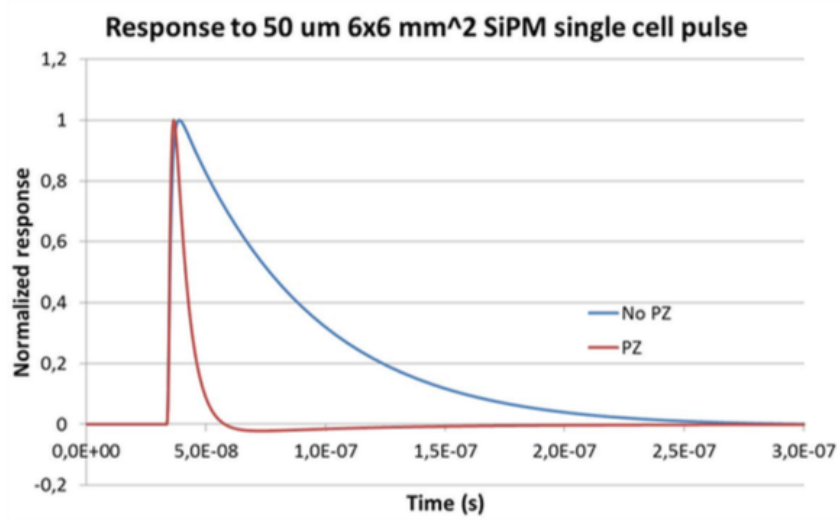

Figure 14: Example of a typical signal of $\tau \approx 40$ ns with and without pole-zero cancellation. [14].

This will give rise to a *time-walk* effect which will need to be corrected for (see section 4.2).

18

3 Experimental Approach

3.1 Linking time of arrival to masses of particles

The momentum of the particles is a known quantity, which possesses a certain uncertainty which will be extracted in section 5.3 and explained in 3.3, it is noted: p. Other known quantities are: the distance between the two chronometers, noted L and the time of flight, Δt (its uncertainty is discussed in section 3.3). The average speed of the particles is thus given by: $v = \frac{L}{\Delta t}$. Knowing that the momentum is given by: $p = mv = $ constant, one can deduce that:

$$\Delta t \text{ large} \implies v \text{ small} \implies m \text{ large},$$

in order to keep p constant. Thus the location of the points (corresponding to each individual particle) on a graph of the amplitude as a function of the time of flight can be estimated: slow particles (long time of flight) are heavy and fast ones are light.

In order to identify the particles, their time of flight will be linked to their corresponding masses, known to be (in natural units):

$$
\begin{array}{rclrcl}
m_e & = & 0.511 \text{ MeV} & m_e^2 & = & 2.61 \cdot 10^{-7} \text{ GeV}^2 \\
m_\mu & = & 0.106 \text{ GeV} & m_\mu^2 & = & 1.12 \cdot 10^{-2} \text{ GeV}^2 \\
m_\pi & = & 0.140 \text{ GeV} & m_\pi^2 & = & 1.96 \cdot 10^{-2} \text{ GeV}^2 \\
m_K & = & 0.494 \text{ GeV} & m_K^2 & = & 2.44 \cdot 10^{-1} \text{ GeV}^2 \\
m_p & = & 0.938 \text{ GeV} & m_p^2 & = & 8.80 \cdot 10^{-1} \text{ GeV}^2
\end{array}
$$

Histograms of the number of events as a function of the mass squared will be produced. It is obtained by converting the time of flight to a mass squared using the following formula (a full derivation can be found in the Appendix, section 8.1):

$$\frac{m^2}{p^2} = \left(\frac{c\Delta t}{L}\right)^2 - 1 \tag{1}$$

Where on the left hand side of the equality there is a dimensionless ratio, as natural units ($c = 1$) are used for m^2 and p^2 and on the right hand side, the inverse velocity is multiplied by $c = 2.997 \cdot 10^8$ m/s so to match the dimension since the time and distance are measured in SI units.

Concerning the time of flight, Δt, for the PMT (S_1 and S_2): $\Delta t = t_2 - t_1 - t_0$ with $t_0 = 83.15$ ns. Similarly for the SiPM (S_3): $\Delta t = t_3 - t_1 - t_0$, with $t_0 = 146.2$ ns. t_0 is determined such that Δt is centered at zero for the electron (positron) peak, i.e. for the PMT electrons (positrons), $t_2 - t_1 = t_0$, similarly for the SiPM electrons (positrons), $t_3 - t_1 = t_0$.

The lengths, L, between the chronometers (i.e. PMT or SiPM detectors), are noted as following, for PMT ($|S_1 - S_2|$): $L = 16.83$ m and for SiPM ($|S_1 - S_3|$): $L = 24.54$ m.

3.2 Predicted time delay

Using equation (1) and solving for Δt, the time which the particles will take to travel from one detector to another, can be predicted, i.e. from S_1 to S_2 for the PMT detector and from S_1 to S_3 for the SiPM detector. Solving equation (1) for Δt, one obtains:

$$\Delta t = \frac{L}{c}\sqrt{\frac{m^2}{p^2} + 1} \tag{2}$$

L is divided by c in SI units to have the time already in s, as $[L] = $ m. The different momenta that will be analyzed are, in GeV: 0.3, 0.6, 0.7, 0.8, 1.0 and 5.0. From now on the time of flight Δt in equation 2 is noted as: t.

The *predicted time delay* refers to the delay in time it will take the muons, pions and protons to arrive to the detector in question as opposed to the positrons (or electrons). This quantity is noted: $\Delta t_i(S_j - S_1) = |t_e - t_i|, i = \mu, \pi, p$ and $j = 2, 3$. Positrons (electrons) are chosen as the reference time because they are ultra-relativistic even if they lose energy during the flight and will therefore keep the same speed throughout the different values of p, actually $v_e \approx c$.

The time of flight: t_i, and the predicted time delay (p.t.d): $\Delta t_i(S_j - S_1)$, are summed up in the two tables below. Table 2 for the PMT, the distance travelled during time of flight being $|S_1 - S_2|$ = 16.83 m and table 3 for the SiPM, the distance travelled during time of flight being $|S_1 - S_3|$ = 24.54 m.

Momentum [GeV]	ToF and p.t.d [ns]	e	μ	π	p
0.3	$t_i = t_{S_2} - t_{S_1}$	56.10	59.49	62.28	184.17
	$\Delta t_i(S_2 - S_1) = |t_e - t_i|$	0.00	3.39	6.18	128.07
0.6	$t_i = t_{S_2} - t_{S_1}$	56.10	56.97	57.95	104.12
	$\Delta t_i(S_2 - S_1) = |t_e - t_i|$	0.00	0.87	1.85	48.02
0.7	$t_i = t_{S_2} - t_{S_1}$	56.10	56.74	57.55	93.80
	$\Delta t_i(S_2 - S_1) = |t_e - t_i|$	0.00	0.64	1.45	37.70
0.8	$t_i = t_{S_2} - t_{S_1}$	56.10	56.59	57.29	86.46
	$\Delta t_i(S_2 - S_1) = |t_e - t_i|$	0.00	0.49	1.19	30.36
1.0	$t_i = t_{S_2} - t_{S_1}$	56.10	56.41	56.65	76.92
	$\Delta t_i(S_2 - S_1) = |t_e - t_i|$	0.00	0.31	0.88	20.82
5.0	$t_i = t_{S_2} - t_{S_1}$	56.10	56.11	56.46	57.08
	$\Delta t_i(S_2 - S_1) = |t_e - t_i|$	0.00	0.01	0.36	0.98

Table 2: Table of predicted time delay of particles for PMT obtained using equation 2, submitting the distance travelled: $L = 16.83$ m.

As expected, the time of flight of the protons (the time it takes them to go from S_1 to S_2) is longer than that of, in decreasing order, pions, muons and positrons. Hence the time delay is the longest for the protons because they travel the slowest, due to their large mass. It can also be concluded that the time of flight is shorter for a particle of higher momentum than the same species of lower momentum. This is expected since higher momentum implies higher speed. The time of flight of electrons doesn't change within the momentum range analyzed. This is because the electrons are ultra-relativistic and travel close to the speed of light throughout the different momenta.

Momentum [GeV]	ToF and p.t.d [ns]	e	μ	π	p
0.3	$t_i = t_{S_3} - t_{S_1}$	81.80	86.74	90.27	268.55
	$\Delta t_i(S_3 - S_1) = |t_e - t_i|$	0.00	4.94	8.47	186.75
0.6	$t_i = t_{S_3} - t_{S_1}$	81.80	83.06	84.00	151.81
	$\Delta t_i(S_3 - S_1) = |t_e - t_i|$	0.00	1.26	2.20	70.01
0.7	$t_i = t_{S_3} - t_{S_1}$	81.80	82.73	83.42	136.78
	$\Delta t_i(S_3 - S_1) = |t_e - t_i|$	0.00	0.93	1.62	54.98
0.8	$t_i = t_{S_3} - t_{S_1}$	81.80	82.51	83.04	126.06
	$\Delta t_i(S_3 - S_1) = |t_e - t_i|$	0.00	0.71	1.24	44.26
1.0	$t_i = t_{S_3} - t_{S_1}$	81.80	82.26	82.60	112.16
	$\Delta t_i(S_3 - S_1) = |t_e - t_i|$	0.00	0.46	0.80	30.36
5.0	$t_i = t_{S_3} - t_{S_1}$	81.80	81.82	81.83	83.23
	$\Delta t_i(S_3 - S_1) = |t_e - t_i|$	0.00	0.02	0.03	1.43

Table 3: Table of predicted time delay of particles for SiPM obtained using equation 2, submitting the distance travelled: $L = 24.54$ m.

From table 3 one notes that the time of flight is longer for the SiPM (compared to PMT) since the distance $|S_1 - S_3|$ is longer than that of $|S_1 - S_2|$. The same conclusions as for Table 2 can be made.

3.3 Uncertainty treatment

This subsection will discuss the treatment of uncertainties of the physical quantities extracted in this project, namely the time of flight, t, and the mass (squared), m^2, of the particles in question. An equation for the uncertainty in mass squared will be derived which will allow for identification of the uncertainties of its independent variables (p, t and L).

In order to find the uncertainty of m^2, equation 1 is used. The time and length are set to natural units to simplify the calculations, i.e. $[t] = [L] = \text{GeV}^{-1}$ [q]. Equation 1 in natural units is:

$$m^2 = p^2 \left(\frac{t^2}{L^2} - 1 \right) \tag{3}$$

In the interest of finding δ_{m^2}, the total derivative of p, t and L will have to be made as their measurements possess a certain individual uncertainty. Taking the total derivative of equation 3 one finds (more detailed steps can be found in the Appendix 8.2):

$$\delta_{m^2} = 2m^2 \frac{\delta_p}{p} + 2E^2 \frac{\delta_t}{t} - 2E^2 \frac{\delta_L}{L} \tag{4}$$

Squaring both sides of equation 4, using: $\delta_i \delta_j = 0$ for $i, j \in \{p, t, L\}$, since they are independent of one another and finally changing the notation: $\delta \equiv \sigma$, one obtains for equation 4:

$$\sigma_{m^2} = 2 \left[m^4 \left(\frac{\sigma_p}{p} \right)^2 + E^4 \left(\left(\frac{\sigma_t}{t} \right)^2 + \left(\frac{\sigma_L}{L} \right)^2 \right) \right]^{\frac{1}{2}}$$

In general, $\frac{\sigma_L}{L} << \frac{\sigma_p}{p}, \frac{\sigma_t}{t}$, and so the uncertainty of the mass squared will be given by:

$$\sigma_{m^2} = 2 \left[m^4 \left(\frac{\sigma_p}{p} \right)^2 + E^4 \left(\frac{\sigma_t}{t} \right)^2 \right]^{\frac{1}{2}} \tag{5}$$

By fitting graphs of the number of events as a function of the mass squared and the number of events as a function of the time flight with a Gaussian, the uncertainty in m^2 (σ_{m^2}) can be determined for each of the particle species (section 5.2); and the uncertainty in the time measurement (σ_t) can be obtained using electrons and positrons because their speed does not depend on the momentum (section 5.1). Actually, the $m^4 \left(\frac{\sigma_p}{p} \right)^2$ term in equation 5 vanishes for small m. Using equation 5 and comparing σ_{m^2} and σ_t the uncertainty in the momentum, σ_p will be deduced (section 5.3).

---

[q]$1 \text{ GeV}^{-1} = 6.5823 \cdot 10^{-25} \text{ s} = 1.9733 \cdot 10^{-16} \text{ m}$

4 Analysis and Results

4.1 Amplitude vs. predicted time delay graphs

The first distributions that will be analyzed are: amplitude as a function of the predicted time delay (p.t.d). The particles will first pass S_1, then S_2 and lastly S_3 (see figure 3). When struck by a particle the counters will give off a signal, at a certain time (expressed in ns), which corresponds to an amplitude (expressed in volts). The difference in time between the arrival at S_1 and S_2 or S_1 and S_3 is equal to the time of flight of the particle. The distributions here below will show the difference in the time of flight of the muons, pions and protons respectively, compared to that of the positrons. Hence they will show the predicted time delay. Using the notation from section 3.2, the p.t.d is expressed as: $\Delta t_i(S_j - S_1) = |t_e - t_i|, i = \mu, \pi, p$ and $j = 2, 3$. The value of the signal (the amplitude) is proportional to the number of photons ejected from the energy deposition of the particle. Therefore a higher amplitude implies a higher energy deposition. Recalling what was discussed in section 3.1, a long time of flight implies a heavier particle and vice versa for short time of flight and lighter particles.

Below an example[r] of a graph of amplitude vs. p.t.d $(\Delta t(S_2 - S_1))$ for the 1.0 GeV positive beam sample for PMT channel 1 is shown:
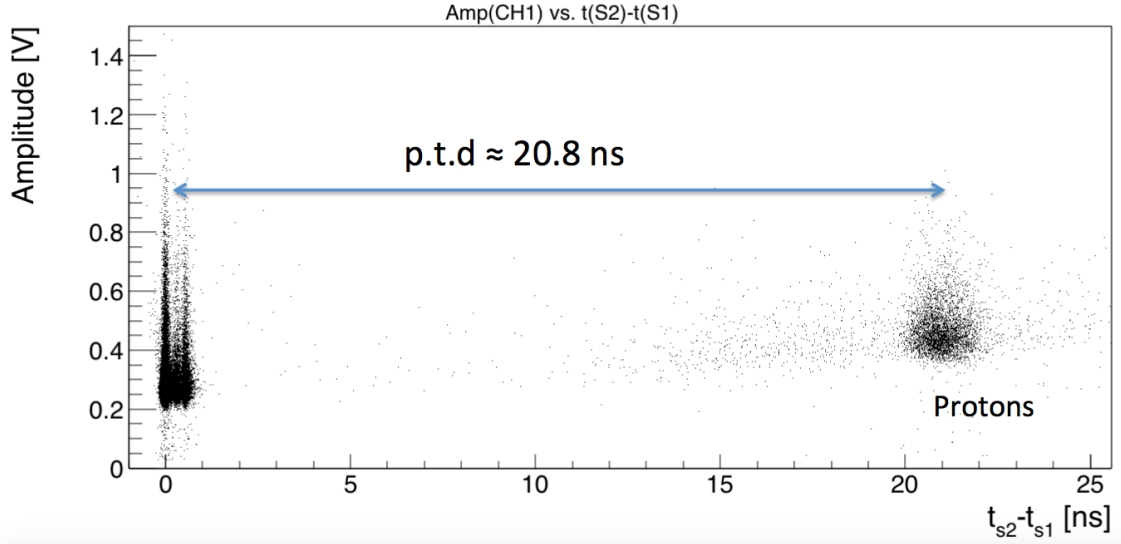

Figure 15: Amplitude vs. predicted time delay for PMT channel 1 (1.0 GeV positive beam), showing positrons, muons, pions and protons and predicted time delay between protons and positrons.

The heaviest particle that is expected to be observed is the proton. Hence the cloud of points between $20 - 25$ ns, with the longest time of flight, corresponds to protons. Using the same logic, lighter particles such as positrons, muons and pions correspond to the points around $0 - 1$ ns. One should note that the points furthest to the left are positrons, as opposed to electrons, as the analyzed beam is a positive one, thus only positively charged particles are in it, i.e: e^+, μ^+, π^+, p.

Figure 15 shows that protons have a higher base amplitude than the other particles. This is due to the fact that the average proton deposits more energy in the detectors than the average e^+, μ^+ and π^+. This can be understood from the Bethe-Bloch formula which expresses the stopping power $\left(\frac{dE}{dx}\right)$ of a uniform medium for a heavy charged particle. Essentially the link between the stopping power and the velocity of the particle in question is[s]: $\frac{dE}{dx} \propto \frac{1}{\beta^2}, \beta = v/c$. Since the proton is heavier, it will travel slower (see section 3.1) and so: $\beta_p < \beta_i, i = e, \mu, \pi \Rightarrow \frac{dE_p}{dx} > \frac{dE_i}{dx}$. Thus the proton will,

---

[r]The same plots are be obtained using the other channels for PMT so to avoid repetition only channel 1 is shown.
[s]For $v < c$

on average, deposit more energy than the average e^+, μ^+ and π^+.

The distributions are made such that the time of flight of the electron is at on average[t] 0 ns, to easier visualize the predicted time delay (p.t.d) of the other particles. This is to say, t_0 is set to a certain value (see section 3.1). On the graph is noted a *rough* estimate of the p.t.d of the protons: $\approx 20.8 \pm 0.1$ ns. *Rough*, because the value of $\Delta t_p(S_2 - S_1)$ is found by hand on the graph, choosing an approximate average of the spread of points using *'Event Statusbar'* in *ROOT*. Additionally, the spread of the protons is fairly wide as there are quite a few points already around 15 ns up to around 25 ns. Thus an error of ± 0.1 ns is estimated in this manipulation. It is interesting to compare the experimental p.t.d (noted Δt_{exp}) with the theoretical (noted Δt_{th}) one that was calculated in section 3.2 and noted in table 2 (as $\Delta t_p(S_2 - S_1)$).

$$\begin{cases} \Delta t_{th} = 20.7 \text{ ns} \\ \Delta t_{exp} = 20.8 \pm 0.1 \text{ ns} \\ \text{Relative \% uncertainty} : 0.5\% \end{cases}$$

Given that the experimental p.t.d has a relative percentage uncertainty of 0.5 %, it can be considered very *precise*. It can also be considered *accurate* as the theoretical value falls within the range of uncertainty ($20.8 - 0.1$ ns $= 20.7$ ns).

Looking closely around 0 ns on figure 15, one can distinguish three separate clouds of points, which should theoretically (from table 2) correspond to positrons, muons and pions, respectively. To see if they can be distinguished, a zoom in of the graph of figure 15 is done:
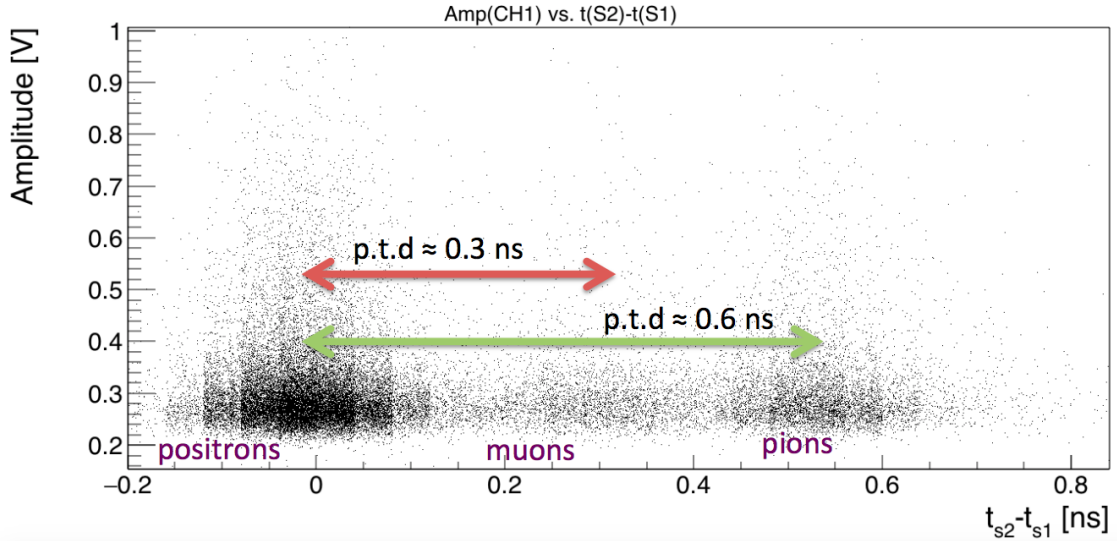

Figure 16: Amplitude vs. predicted time delay for PMT channel 1 (1.0 GeV positive beam), showing positrons, muons and pions and predicted time delay between muons/pions and positrons.

Thus the lighter particles can clearly be distinguished, thanks to the excellent time resolution of our counters (see section 5.1 for more detail).

A first remark to make is that a higher number of positrons than muons and pions are detected. It will now be explained why. In figure 4 the fractional composition of the beam *just after* the

---

[t]On average, because the points are are spread out from one another, so the average of the spread of points is set at 0 ns.

production target is plotted from Monte Carlo simulations. From which it can be concluded that a positive beam at 1.0 GeV expects the same amount of pions (π^+) as positrons. Figure 16 indicates particles arriving *far after* the production target. The pions in the beam are not stable and so some of them will disintegrate during the time of flight into muons[u]. Positrons are fundamental particles and so will not disintegrate. Hence the fewer amount of pions (and muons) as compared to positrons. Kaons are not observed (although figure 4 suggests so) because they too will decay, into either $\mu + \nu_\mu$ or $\pi + \pi^0$. Their lifetime, in their frame of reference (i.e. at rest) is, on average, $\approx 10^{-8}$ s = 10 ns, or in terms of the *decay length*, they will disintegrate (in their frame of reference) after, on average, 3.711 m. However according to laboratory observers, kaons will have a delayed lifetime and hence longer decay length, since they travel to speeds close to that of light and time dilation so has to be taken into account. Actually for kaons in a beam of 1 GeV, the laboratory observers consider the decay length to be 8.39 m (for detailed steps see the Appendix section 8.3). Since the counters S_1/S_2 and S_1/S_3 are separated of 16.83 m and 24.54 m respectively, the kaons will decay before arriving to the second counter in both configurations, therefore no kaons are observed.

Once again, the corresponding predicted time delays are noted on the figure (16). They are easier to extract than that of the protons since the mean point of their spread is quite visible, hence no relevant uncertainty is taken into account. One notes that these values are exactly the same as those found from the theoretical calculations in section 3.2, noted in table 2.

The same is done for the 1.0 GeV positive beam sample for the SiPM detector, for channel 7, as an example. The amplitude as a function of the predicted time delay ($\Delta t(S_3 - S_1)$) is shown below:
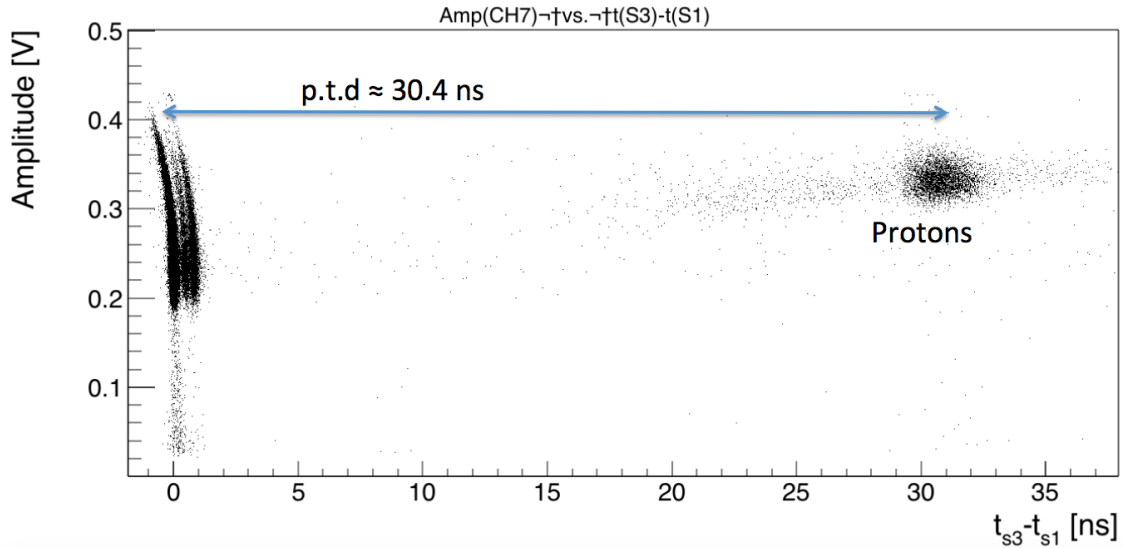

Figure 17: Amplitude vs. predicted time delay for SiPM channel 7 (1.0 GeV positive beam), showing positrons, muons, pions and protons and predicted time delay between protons and positrons.

The same reasoning as before is applied to understand that the cloud of points at higher times of flight corresponds to protons and at lower times of flight, positrons (and muons and pions). Once again the predicted time delay is noted for the protons. The experimental p.t.d corresponds perfectly to the theoretical one (see table 3).

Looking carefully at figure 17 one notices that the events tend to go towards earlier times after a certain amplitude (≈ 0.3 V), i.e. a slight bend can be seen. In order to better understand this phenomenon and to distinguish the lighter particles from each other, a zoom in of figure 17 is done

---

[u]Muons can also be produced from cosmic rays interacting with the atmosphere arriving onto the detector.
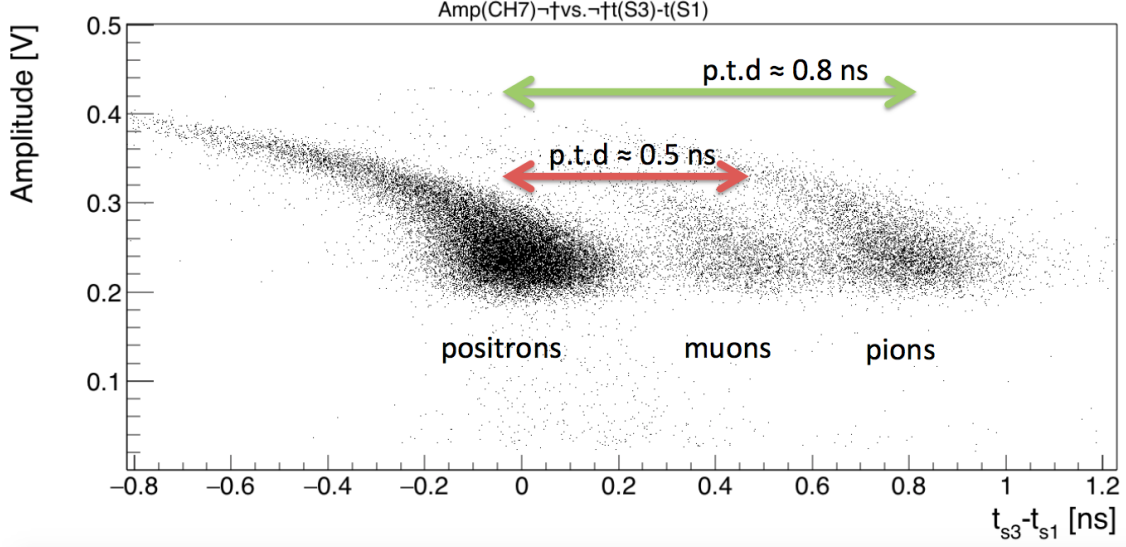
around short times of flight.

Figure 18: Amplitude vs. predicted time delay for SiPM channel 7 (1.0 GeV positive beam), showing positrons, muons and pions and predicted time delay between muons/pions and positrons.

The lighter particles can also in this case be distinguished (again, thanks to the excellent time resolution of the counters, see section 5.1). The predicted time delays are noted, which once again correspond perfectly to their respective theoretical values (see table 3).

The effect of events going towards earlier times after a certain value of amplitude and so resulting in a bend in the set of points is seen very clearly now. This is the so-called *time-walk* effect which, in this case, is purely due to the signal distorsion in the electronics of the SiPM detector (see section 2.8). A vertical line of points is wanted when analyzing, like the PMT case (see figures 15 and 16), hence a correction is needed.

4.2 Time-walk correction of SiPM

The idea of the correction is to take the events that don't follow the vertical line trend and place them so as to follow it. Firstly, the set of points (the events) are approximated to a polynomial function, of fourth degree, which is therefore characterized by five different parameters. The following function is used for channel 7[v]:

$$t_{fit}(x) = a + b \cdot x + c \cdot x^2 + d \cdot x^3 + e \cdot x^4 \tag{6}$$

Where $x = Amp[7]$, from the notation in the program for the value of the amplitude. The parameters of equation 6 obtained from the fit of the histogram are:

a = 63.4299

b = 25.453

c = -150.35

d = 363.638

e = -273.137

---

[v]The same is done for channel 6, with other parameters.

In order to obtain the corrected time, i.e. a straight line of events, the following equation is applied:

$$t_{corrected}(x) = t_1 - t_3 - t_{fit}(x) + 65 \qquad (7)$$

Where the term: $+ 65$, comes from taking the average of $t_{S_3} - t_{S_1}$ at low values of amplitude (see figure 19). It should be noted that to find the fit only one species of particles is used (i.e. one set of points). This doesn't cause any problem as the effect (*time-walk*) is independent of the nature of the particle and will so cause the same bend for all different types. The chosen species to do the fit are positrons as they can be easily separated from the rest thanks to the Cherenkov detector. At 1.0 GeV they are the only particles that emit Cherenkov radiation (see figure 5).

The graphs of figures 19 and 20 shown below correspond to uncorrected and corrected versions respectively of the time of flight as a function of the amplitude[w], for positrons selected to provide signals in the Cherenkov detector for SiPM channel 7.
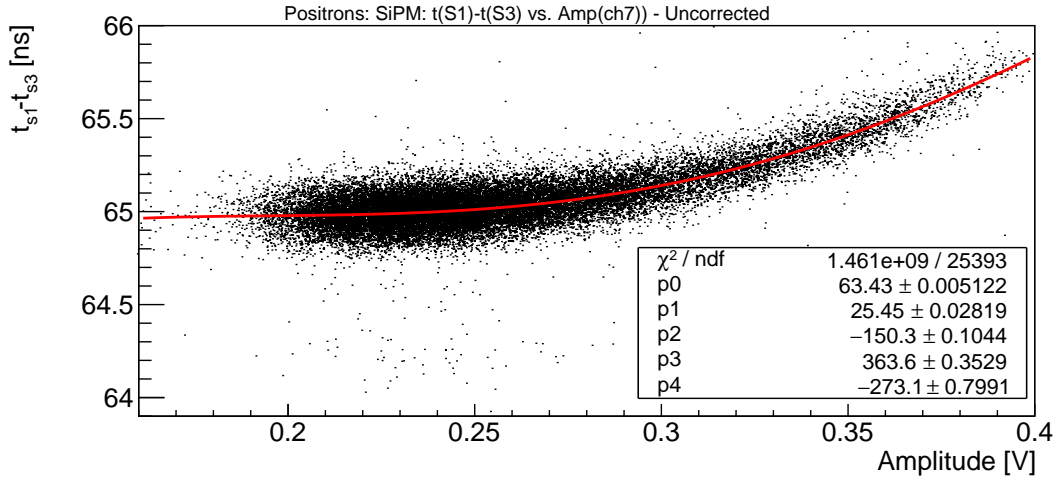

Figure 19: Uncorrected graph of the time of flight vs. amplitude for the positrons of SiPM channel 7 (1.0 GeV positive beam) with fitted function $t_{fit}(x)$ plotted.

It can be concluded that $t_{fit}(x)$ follows well the set of points and is thus a good choice of fit.

---

[w]NB. the axis are changed as opposed to the previous section 4.1.
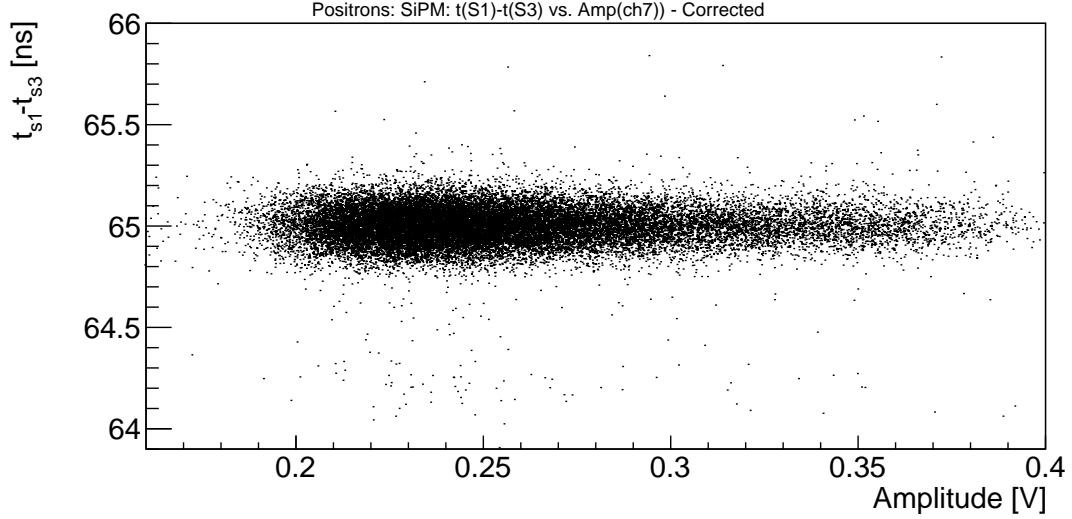
Figure 20: Corrected graph of the time of flight vs. amplitude for the positrons of SiPM channel 7 (1.0 GeV positive beam).

The distribution no longer has a bend after a certain amplitude and so all points can be associated to the same time of flight. One can thus conclude that the applied correction works. This correction (equation (6)) is used in all analysis of SiPM data (eg. for finding the mass of the particles too). In the figure below (fig. 21) corrections for positrons, muons and pions are shown together, confirming hence that the correction is independent of the nature of the particle.
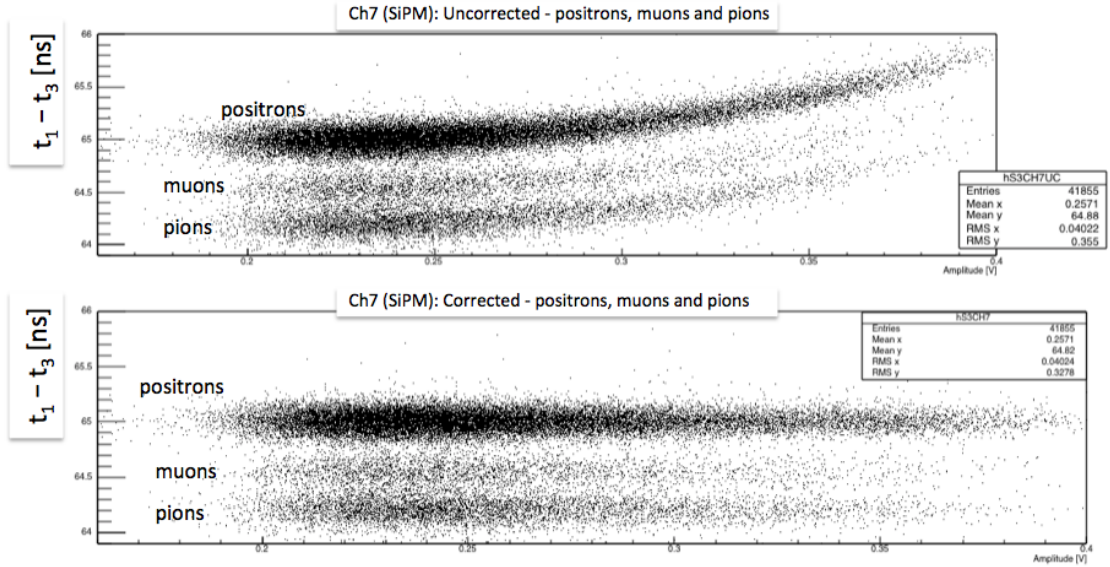

Figure 21: Uncorrected (top) and corrected (below) graphs of the time of flight vs. amplitude for positrons, muons & pions of SiPM channel 7 (1.0 GeV positive beam).[x]

---

[x]NB: The correction for time is such that positrons arrive "later" than the muons and pions, since $t_1 - t_3$ is used and no other corrections. In section 4.3 Δt_e is set to be ≈ 0 ns to get the correct m^2.

4.3 Identification of the mass (squared)

In this section the mass squared (m^2) distribution of the particles will be determined from the time distribution which has been found earlier: the time of flight of the particles (Δt) and the correction of the SiPMs. For a given momentum[y], Δt of the particle in question will be linked to its m^2 through equation (1). The same channels as before will be analyzed (i.e. Ch1 for S_2 and Ch7 for S_3).

An iteration over events of a positive beam run in July 2018 has been made for different values of momentum. Each respective value will give a histogram of the number of events as a function of the mass squared. Histograms for $0.3, 0.6$ and 1.0 GeV data will be shown and histograms for 0.7 and 0.8 GeV data are found in the appendix (section 8.4) to avoid repetition. The histograms of the number of events vs. m^2 of PMT and SiPM will be analyzed separately (sections 4.3.1 and 4.3.2, respectively). Similar histograms will be analyzed for a beam of a momenta of 5.0 GeV in section 4.3.3. A separate section for this data is chosen because at this value of momenta kaons will be observed (as opposed to the other momenta in sections 4.3.1 and 4.3.2). In section 4.3.4, positive and negative beams will be compared to each other for momenta of 1.0 and 5.0 GeV.

---

[y]It is supposed fixed for now, see section 5.1 and 5.2 for its uncertainty extraction.

4.3.1 Mass extracted from the $|S_1 - S_2|$ counter

Below histograms of the number of events as a function of the mass squared are shown for particles going from S_1 to S_2. A positive beam is analyzed, hence positrons, muons (μ^+), pions (π^+) and protons can be seen for the given momenta (0.3, 0.6 and 1.0 GeV).
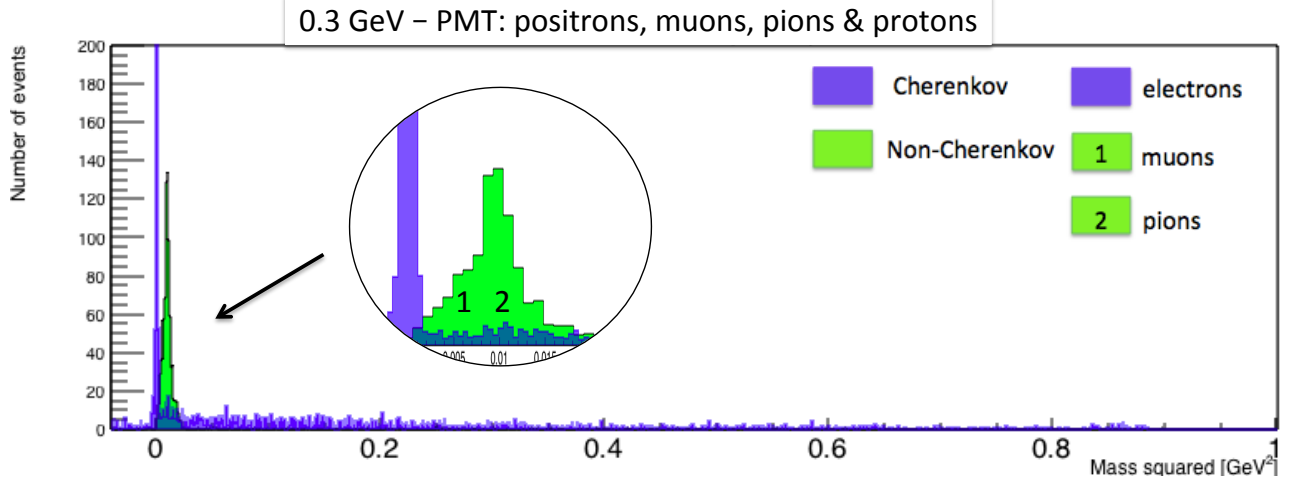

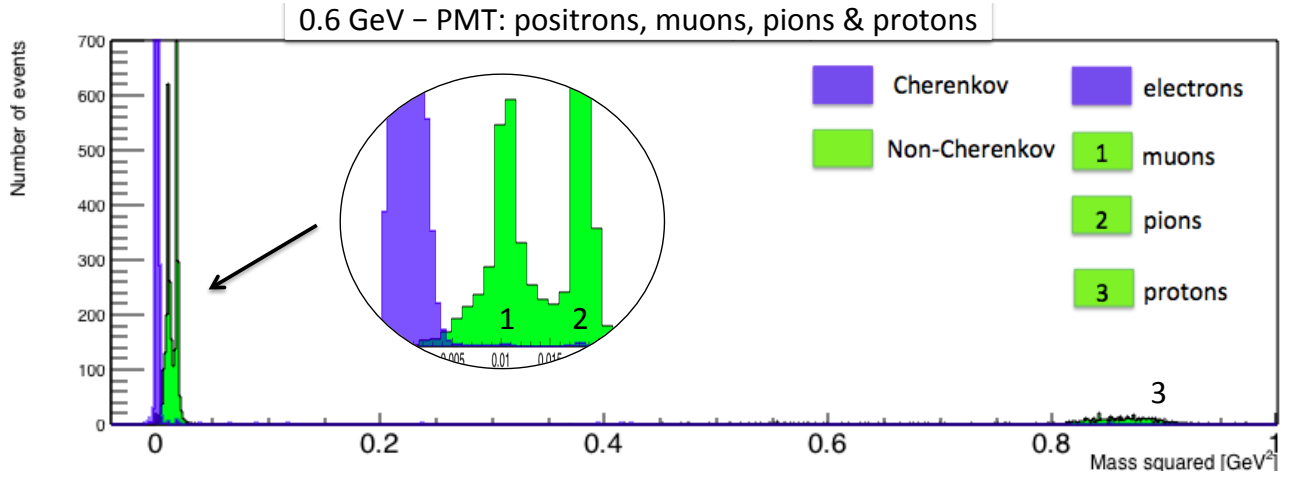Figure 22: Number of events vs. m^2 calculated from $t_{S_2} - t_{S_1}$ at $p = 0.3$ GeV.

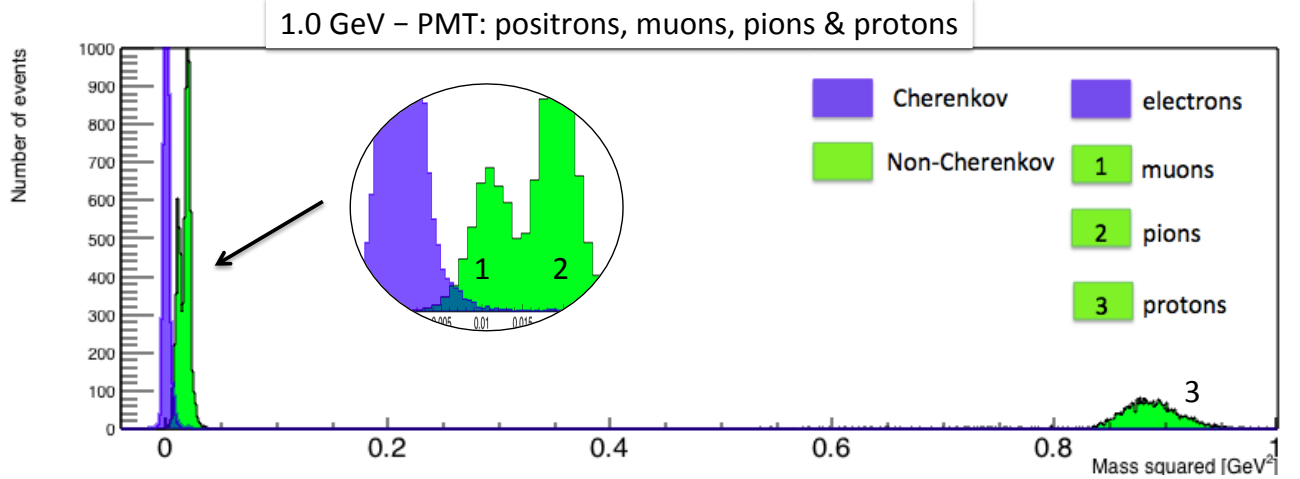Figure 23: Number of events vs. m^2 calculated from $t_{S_2} - t_{S_1}$ at $p = 0.6$ GeV.

Figure 24: Number of events vs. m^2 calculated from $t_{S_2} - t_{S_1}$ at $p = 1.0$ GeV.

The three histograms (figures: 22, 23 and 24) are placed on top of each other, with the same scale on the x-axis (m^2-axis) in order to conveniently compare them.

A first remark to make is that the positrons can be distinguished from the muons, pions and protons, without any m^2-axis needed. This is because at momenta up to 1.0 GeV there are only positrons that will give off Cherenkov radiation (see figure 5). Hence a different colour can be set for the positrons, allowing for their distinction.

Starting with the proton peak (theoretically at $m_p^2 = 8.80 \cdot 10^{-1}$ GeV^2), one starts by noticing that at 0.3 GeV (fig. 22), there are basically no protons. At this momentum the proton production cross-section is small. From fig. 4 it is seen that their fraction of composition of the beam is low as compared to the other particle species. At 0.6 GeV (fig. 23) a small proton peak emerges, as here the production cross-section is bigger and the fractional composition is slightly larger (see fig. 4). Finally at 1.0 GeV (fig. 24) a clear proton peak can be seen, here the energy of the beam is about the mass of the proton. This latter histogram shows that the peak of the proton is around its theoretical mass at $m_p^2 = 8.80 \cdot 10^{-1}$ GeV^2. A more detailed analysis of this can be found in section 5.2. These conclusions follow well figure 4 that shows the fractional composition of the particles in the beam, just after the production target. It shows clearly that at 0.3 GeV protons are very scarce (nay not existent), becoming more present at 0.6 GeV and lastly at 1.0 GeV can clearly be identified, which corresponds to these experimental results.

Concerning the muons and pions, firstly, as these are results from the whole flight distance, pions have had time to decay into muons. Their mass peaks are confused for $p = 0.3$ GeV (fig. 22) rendering a distinction of them hard. It is believed that at low energy the resolution of the muon mass peak is poor because they have a large spread in momentum, since they are produced in pion decays. At low beam momentum this effect is more pronounced, thus the confusion of mass peaks of muons and pions at 0.3 GeV. At 0.6 GeV (fig. 23) they can clearly be distinguished. This is also the case for 1.0 GeV (fig. 24), where more energy of the beam fills up the histograms with more events as more muons and pions can be produced. The conclusions follow the graph in figure 4, where one can however only see the fraction of pions produced (Monte Carlo simulation done, again, only just after the production target not allowing the pions to have time to decay). It is however clear from the three histograms (figures: 22, 23 and 24) that more pions than protons are produced, which figure 4 also indicates (for momenta of: 0.3, 0.6 and 1.0 GeV). The theoretical masses squared of muons and pions are: $m_\mu^2 = 1.12 \cdot 10^{-2}$ GeV^2 and $m_\pi^2 = 1.96 \cdot 10^{-2}$ GeV^2 which by eye seem to be

at the right location, this will be more closely analyzed in section 5.2.

Lastly, the positron peaks are analyzed. The positrons are ultra-relativistic and so have a distinguished peak at around 0 GeV^2 (the theoretical mass squared being: $m_e^2 = 2.61 \cdot 10^{-7}$ GeV^2) for all three histograms (figures: 22, 23 and 24). The positron peak has a lot of noise for only the $p = 0.3$ GeV histogram (fig. 22), however this is a false appearance because its y-axis of the number of events goes only to 200, as opposed to 700 and 1000 events for the other two (figures 23 and 24). Meaning that this is the case for them as well, just that the scale of their axis doesn't allow for it to be seen. The so called *noise*, or in other terms, the peaks of m_e^2 at masses (squared) which do not correspond to the theoretical one is most likely due to the secondary production of $e^{\pm}$ from scattering of other particles in the beam, which in turn will give signals in the Cherenkov detector. For example, a pion that interacts just before the Cherenkov counter and produces a positron (or electron) would be tagged as a positron by the Cherenkov detector and produce a peak at the expected position of the pion mass squared peak. Interestingly enough, this is exactly what can be seen in figure 23. A small bump of positrons are visible at the pion peak. Yet again the conclusions fit with figure 4, showing that more positrons are produced than muons, pions and protons (for the analyzed momenta). However, at 1.0 GeV figure 4 shows that the same number pions and positrons are produced, which is not the case for these histograms (there are more positrons than pions). This is again because some pions have decayed into muons.

In conclusion, the formula for converting the time of flight to the mass squared (equation 1) is correct since the the mass squared peaks of the particles correspond by eye to the theoretical ones. Thus there is knowledge of how to produce histograms of the number of events as a function of the mass squared and so the Time-of-Flight detector (comprising S_1 and S_2) allows for particle identification. Its uncertainty in the mass squared will be discussed in section 5.2, where an evaluation of its capacity of PID will be addressed.

4.3.2 Mass extracted from the $|S_1 - S_3|$ counter

In this sub-section, particles going from S_1 to S_3 are analyzed, allowing for histograms of the number of events as a function of the mass squared to be produced. Again, a positive beam is analyzed, hence e^+, μ^+, π^+ and p can be seen for the given momenta (0.3, 0.6 and 1.0 GeV).
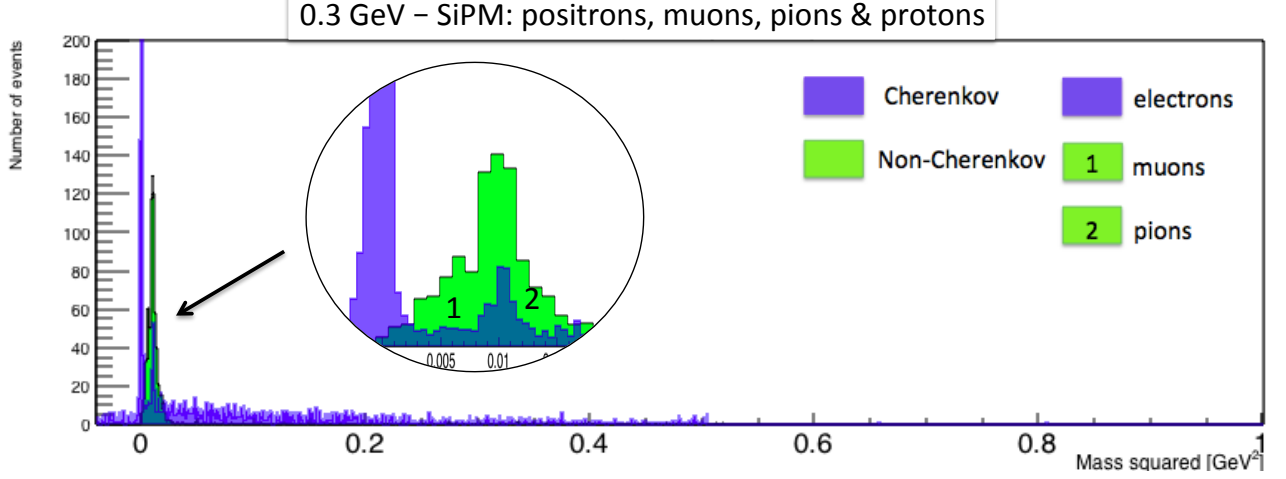

Figure 25: Number of events vs. m^2 calculated from $t_{S_3} - t_{S_1}$ at $p = 0.3$ GeV.
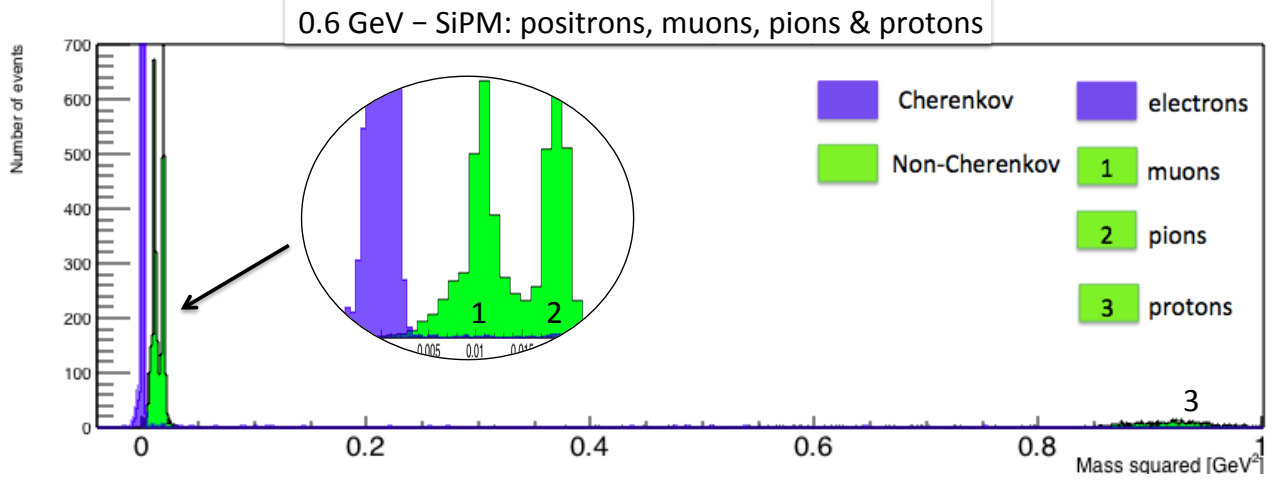

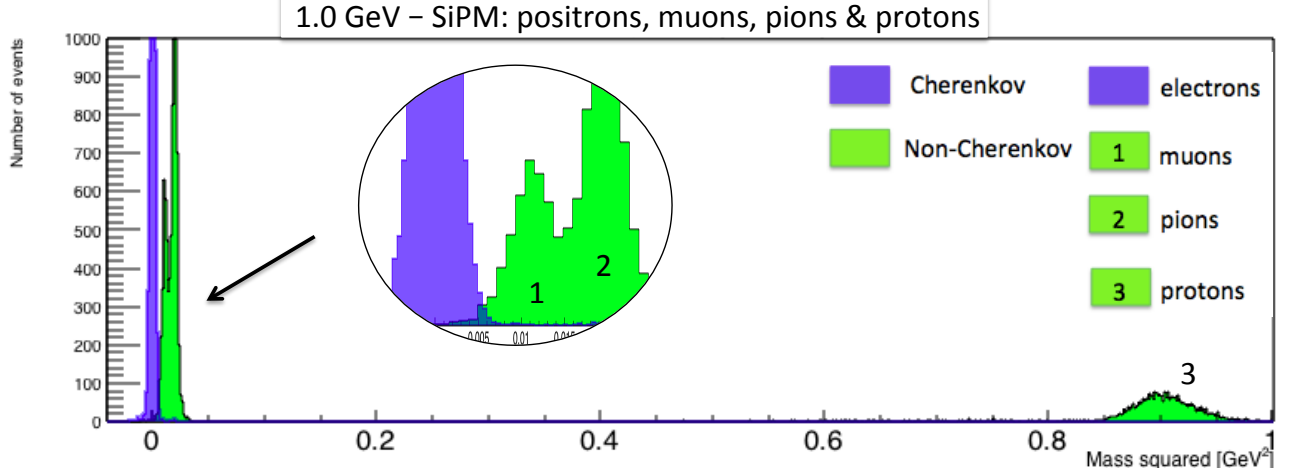Figure 26: Number of events vs. m^2 calculated from $t_{S_3} - t_{S_1}$ at $p = 0.6$ GeV.

Figure 27: Number of events vs. m^2 calculated from $t_{S_3} - t_{S_1}$ at $p = 1.0$ GeV.

The same conclusions as in section 4.3.1 can be made for these histograms (figures: 25, 26 and 27). Concerning the protons, again a mass peak emerges at 0.6 GeV^2 and is clear at 1.0 GeV^2. One important remark to make is that the proton peak seems to be slightly shifted to the right (at higher m^2) in figure 27, as compared to figure 24, hence having an average m^2 not exactly around $m_p^2 = 8.80 \cdot 10^{-1}$ GeV^2, but a bit higher. This is because in between the distance of flight $S_1 - S_3$ (24.54 m) there were some material that hadn't been taken away. Hence when the particles passed there were obstacles they had to traverse which would slow them down. Protons being the heaviest, they are the most affected and so give off a slower time of flight than what is predicted. From equation 1, a longer Δt implies a higher m^2.

Concerning the positrons, muons and pions, there is nothing more to say that hasn't yet been mentioned in section 4.3.1. One remark concerning the noise of the positrons in figure 25 is worth to make. There seems to be slightly more noise than in figure 22, this might come from the extra parts in the way, allowing for a very slight shift to higher m^2.

In conclusion, the correction done for the *time-walk* effect (which is needed for SiPM analysis) is correct and the Time-of-Flight detector comprising S_1 and S_3 allows for particle identification. Yet again, an evaluation of its capacity of PID will be addressed by looking at its uncertainty in the mass squared (see section 5.2). In the following section, the mass determination of beams at 5.0 GeV for PMT and SiPM will be boarded.

4.3.3 5 GeV data

In this subsection histograms of the number of events as a function of the mass squared will be analyzed in the case of positive beam data of momentum 5.0 GeV for both PMT (figure 28) and SiPM (figure 29).
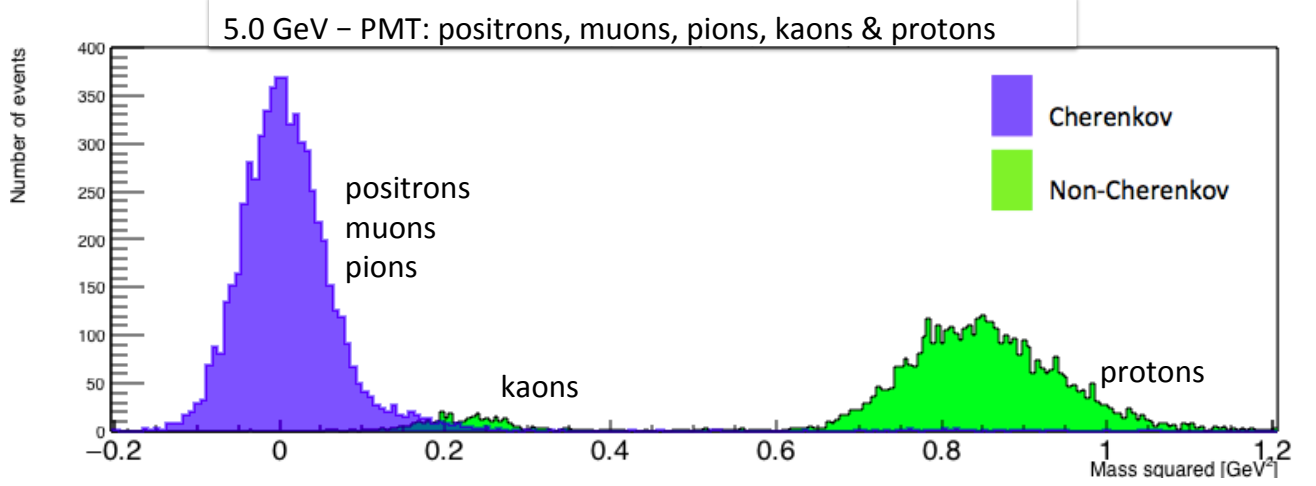

Figure 28: Number of events vs. m^2 calculated from $t_{S_2} - t_{S_1}$ at $p = 5.0$ GeV.
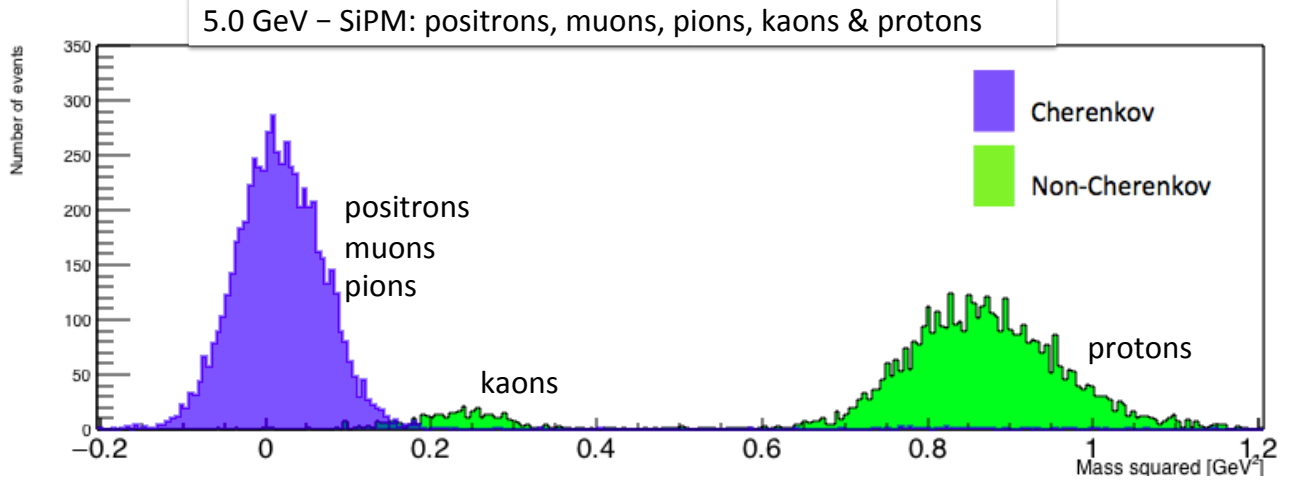

Figure 29: Number of events vs. m^2 calculated from $t_{S_3} - t_{S_1}$ at $p = 5.0$ GeV.

A first remark to make is that not only the same particles as before can be found (e^+, μ^+, π^+ and p) but also kaons, K^+, are observed, as indicated at 5.0 GeV by figure 4. It was discussed in section 4.1 that kaons will, in their frame of reference decay after 3.711 m. However, since they travel with $v \sim c$, time dilation has to be taken into account when calculating the decay length as observed in the laboratory. It is found (see the Appendix section 8.3) that kaons in a beam of 5.0 GeV will decay after 37.1 m. Since the distance between the S_1/S_2 and $S_1/_3$ counters are

16.83 m and 24.54 m, respectively, the kaons in this beam will not decay before reaching the second counters. This explains why there is a K^+ peak emerging in both figures 28 and 29.

Another difference from the previous histograms in sections 4.3.1 and 4.3.2 is that in figures 28 and 29, positrons, muons and pions go under the events of purple colour. Meaning thus that they all emit Cherenkov radiation when passing by the Cherenkov detector on their way to S_2 or S_3. This coincides with the results of graph in figure 5. Hence at $p = 5.0$ GeV these particles cannot be distinguished with the Cherenkov detector. They also have a very high energy as compared to their rest mass and so produce a mass trace at a large range of masses squared (from about -0.2 GeV^2 to 0.2 GeV^2). One notes that, for these particles, events of $m^2 < 0$ GeV^2 are found. This is due to the uncertainty in the timing measurements (see section 5.1), giving hence a Gaussian curve around the average value for their corresponding m^2. A final thing to note is that there are a lot more protons as compared to protons produced in the sections 4.3.1 and 4.3.2, which corresponds well to figure 4. This is because a higher value of momenta allows for more protons to be produced more readily. Figure 4 also indicates a very low value of positrons, which are compensated by the higher number of pions (and so muons) that are expected to be produced. Once again a slight shift towards higher m^2 can be observed for the SiPM histogram (fig. 29) as compared to the PMT histogram (fig. 28). This because of the same reason as discussed in section 4.3.2.

4.3.4 Comparing positive and negative beam files

Here below are histograms of positive and negative beam files for 1.0 GeV and 5.0 GeV. In the negative beam e^-, μ^-, π^- are expected to be seen. Anti-protons ($\bar{p}$) are built up of anti-quarks, thus their production cross-section is much smaller than the one of protons (see fig. 3). In the positive beam e^+, μ^+, π^+ and p can be seen. Figure 30 shows the difference in content of particles of the two beams.
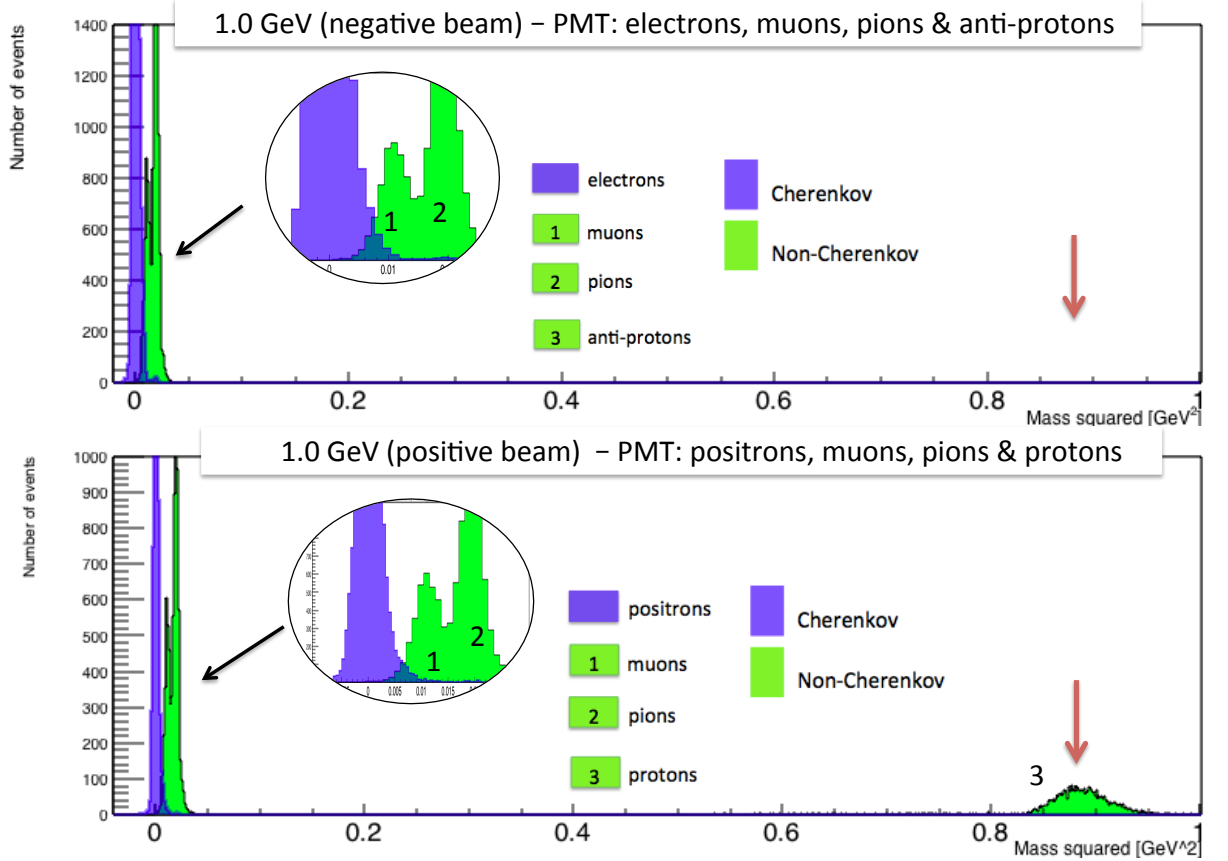

Figure 30: Number of events vs. m^2 of PMT at $p = 1.0$ GeV for a negative and positive beam.

One can safely conclude that there are no anti-protons detected. Anti-protons are stable and could in principle be detected, however as soon as they come in contact with a proton, both will annihilate and become a burst of energy. Concerning the other particles it can be concluded from figure 30 that the masses are equal for particles and anti-particles. Below the same game is done for beams of 5.0 GeV.
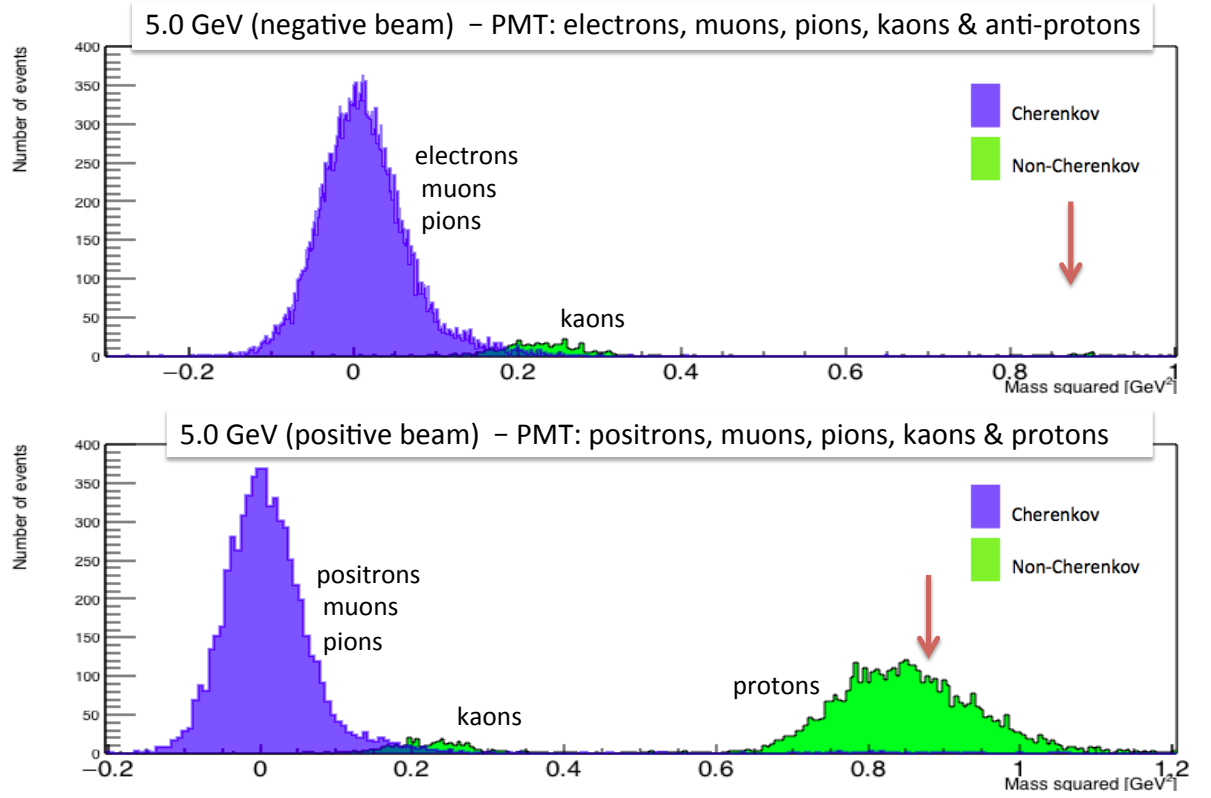
Figure 31: Number of events vs. m^2 of PMT at $p = 5.0$ GeV for a negative and positive beam.

Figure 31 allows for the same conclusions, noticing however that kaons ($K^{\pm}$) are produced too and that $e^{\pm}, \mu^{\pm}$ and $\pi^{\pm}$ give off Cherenkov Radiation. A slight hint of $\bar{p}$ can be spotted in the top mass squared distribution of fig. 31.

5 Uncertainty identification

5.1 Identifying the uncertainty in time

In this sub-section the uncertainty in the timing of the counters S_1, S_2 and S_3 will be identified by fitting distributions of the number of events as a function of the time of flight for *positrons* with a Gaussian curve for a beam of $p = 1.0$ GeV. Positrons are used to find the uncertainty in the timing of the counters since they are ultra-relativistic particles, with hence $v \sim c$. This implies that their distributions will not include any spread in momenta and so show a pure uncertainty in timing.

These distributions will represent a peak, which is used to calculate the mean time of flight of the particle in question. The width of the peak represents the uncertainty of the time of flight between the two counters. Given two counters, σ_i and σ_j, σ is linked to the counters (S_i and S_j) by: $\sigma = \sqrt{\sigma_i^2 + \sigma_j^2}$. Assuming that the uncertainties of the individual counters are the same, one obtains: $\sigma_i = \frac{\sigma}{\sqrt{2}}$, $i \in \{1, 2, 3\}$.

Below the distributions of positrons (fig. 32) and muons and pions (fig. 33) are shown with corresponding *mean* and σ. The distribution of the number of protons as a function of time of flight is not shown as it is not used for the identification in the uncertainty of time. This is because protons are strongly affected by multiple scattering and so will have a relatively larger smear in momentum and so also smear in time of flight, giving high values of σ.
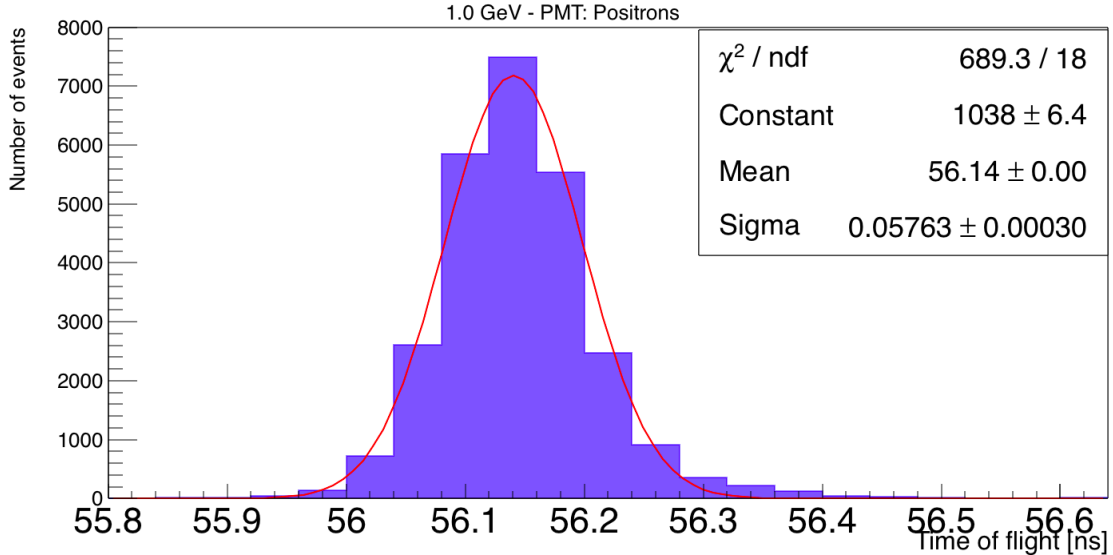

Figure 32: Number of events vs. time of flight between S_1 and S_2 of positrons at $p = 1.0$ GeV with Gaussian fit around mean value of time of flight.

Figure 32 shows an average time of flight of the positrons between S_1 and S_2 of 56.14 ns with a corresponding uncertainty of 58 ps.
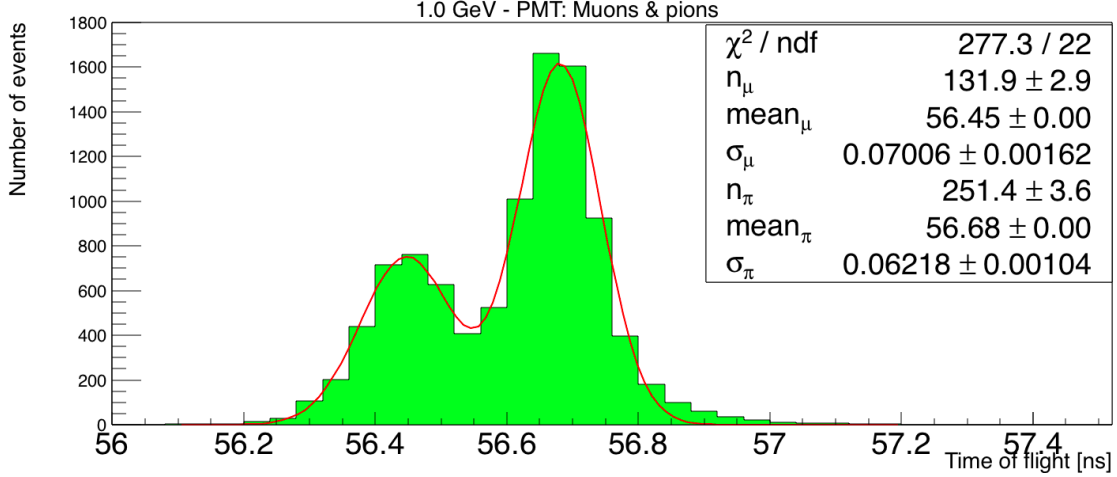
Figure 33: Number of events vs. time of flight between S_1 and S_2 of muons and pions at $p = 1.0$ GeV with corresponding Gaussian fits around their respective mean values of time of flight.

Figure 33 shows an average time of flight of the muons and pions of 56.45 ns and 56.68 ns, respectively. Their corresponding uncertainties being 70 ps and 62 ps.

A summary of the average time of flight and corresponding uncertainty from figures 32 and 33 are shown in table 4 below. The experimental time of flight is noted: $\Delta t_{exp} = t_2 - t_1 - t_0$ and the theoretical one: Δt_{th} (derived in section 3.2 and found in table 2). The uncertainty in the time of flight between S_1 and S_2 is noted: σ.

Particles species	Δt_{exp} [ns]	σ [ps]	Δt_{th} [ns]
e	56.14	58	56.10
μ	56.45	70	56.41
π	56.68	62	56.65

Table 4: Experimental and theoretical time of flight (Δt_{exp} and Δt_{th}) and corresponding uncertainty (σ) of S_1 and S_2 counters, distant of 16.83 m.

It can be concluded that the results of the corresponding experimental times of flight of the three particle species are very accurate, as they lie within the range of $|0.04|$ ns to their corresponding theoretical times of flight. They can also be considered precise as the relative uncertainty of the time of flight is small, more specifically $\frac{\sigma_e}{\Delta t_e} = \frac{58 \cdot 10^{-3}}{56.14} = 0.001 = 0.1\%$. The relative uncertainty of the positrons is used for the reason explained above. The counters S_1 and S_2 can thus be considered very precise. The resolution of the time of flight of muons and pions is poorer than that of the positrons since they are heavier and will so have a contribution to their value of σ from the momentum too. The reason for the resolution in time of flight (σ) of the muons to be the poorest is due to the fact that muons are created in the beam as a result of pion decay which results in an additional spread in momentum.

The same procedure is applied for finding the uncertainty in the time of flight of the particles travelling the distance $|S_1 - S_3|$. The figures 34 and 35 show the mean value of time of flight and its uncertainty, σ for positrons and muons and pions, respectively.
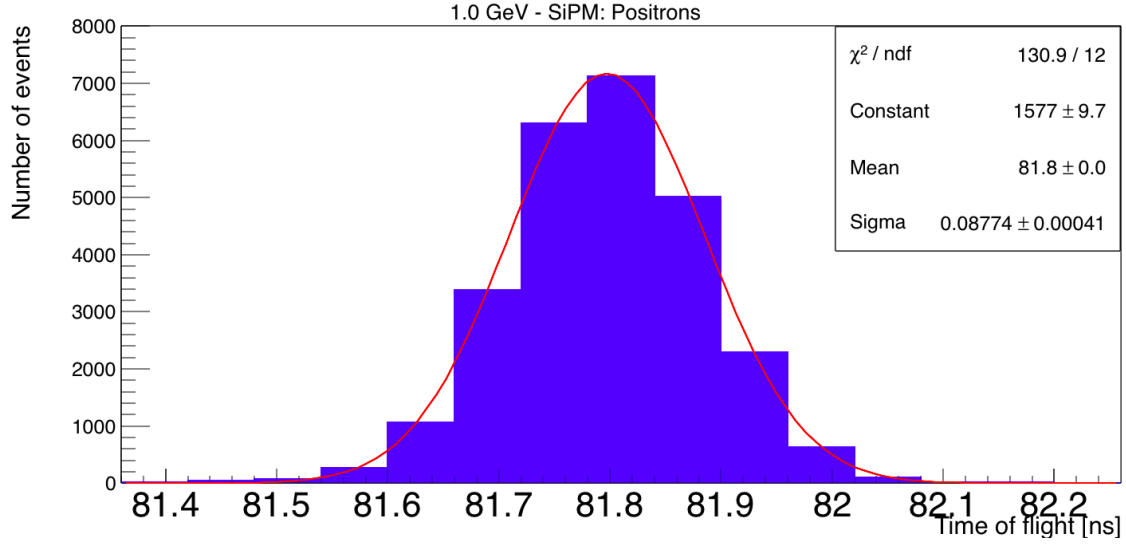
Figure 34: Number of events vs. time of flight between S_1 and S_3 of positrons at $p = 1.0$ GeV with Gaussian fit around mean value of time of flight.

Figure 34 shows an average time of flight of the positrons of 81.80 ns with a corresponding uncertainty of 88 ps.
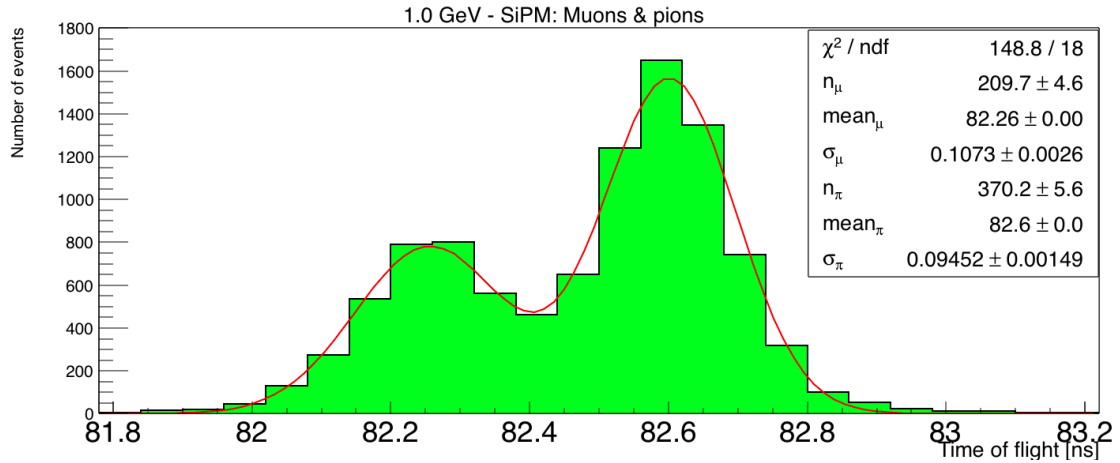

Figure 35: Number of events vs. time of flight between S_1 and S_3 of muons and pions at $p = 1.0$ GeV with corresponding Gaussian fits around their respective mean values of time of flight.

Figure 35 shows an average time of flight of the muons and pions of 82.26 ns and 82.60 ns, respectively. Their corresponding uncertainties being 107 ps and 95 ps.

Again, a summary of the average time of flight and corresponding uncertainty from figures 34 and 35 are shown in table 5 below, noting that: $\Delta t_{exp} = t_3 - t_1 - t_0$ and Δt_{th} corresponds to the theoretical time of flight (derived in section 3.2 and found in table 3). The uncertainty in the time of flight between S_1 and S_3 is noted: σ.

Particles species	Δt_{exp} [ns]	σ [ps]	Δt_{th} [ns]
e	81.80	88	81.80
μ	82.26	107	82.26
π	82.60	95	82.60

Table 5: Experimental and theoretical time of flight (Δt_{exp} and Δt_{th}) and corresponding uncertainty (σ) of S_1 and S_3 counters, distant of 24.54 m.

The same conclusions as before can be made here. The experimental time of flight corresponds exactly to the theoretical one, hence the counters (S_1 and S_3) are very accurate. They are very precise too, since relative uncertainty, again using the one of the positrons for the same reasons as before, is very small. More specifically $\frac{\sigma_e}{\Delta t_e} = \frac{88 \cdot 10^{-3}}{81.80} = 0.001 = 0.1\%$. For the same reason as discussed before the uncertainties in time of flight (σ) of the muons and pions are poorer that that of the positrons (electrons), the muon's being the poorest.

5.2 Identifying the uncertainty in mass squared

In this sub-section the uncertainty in the mass squared will be found. The method is the same as for the previous section (5.1). Hence figures of the number of events vs. the mass squared are produced from data corresponding to a beam of 1.0 GeV for positrons, muons and pions and protons. Furthermore, a Gaussian fit is applied around their mean m^2. Below the mass squared distributions are found for the $|S_1 - S_2|$ configuration (figures 36, 37 and 38) and for the $|S_1 - S_3|$ configuration (figures 39, 40 and 41).
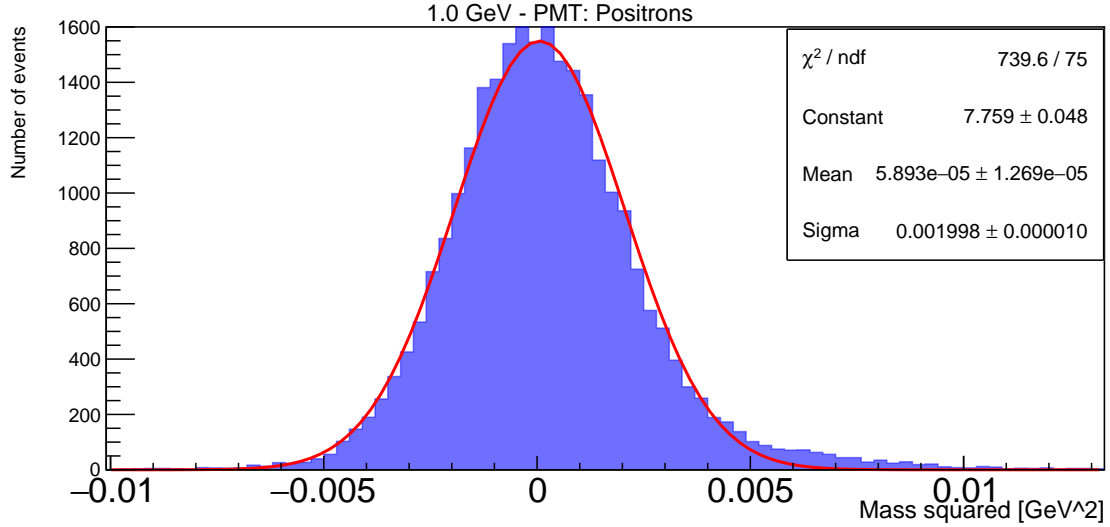

Figure 36: Number of events vs. mass squared of positrons at $p = 1.0$ GeV for the $|S_1 - S_2|$ configuration with corresponding Gaussian fit around mean value of m^2.
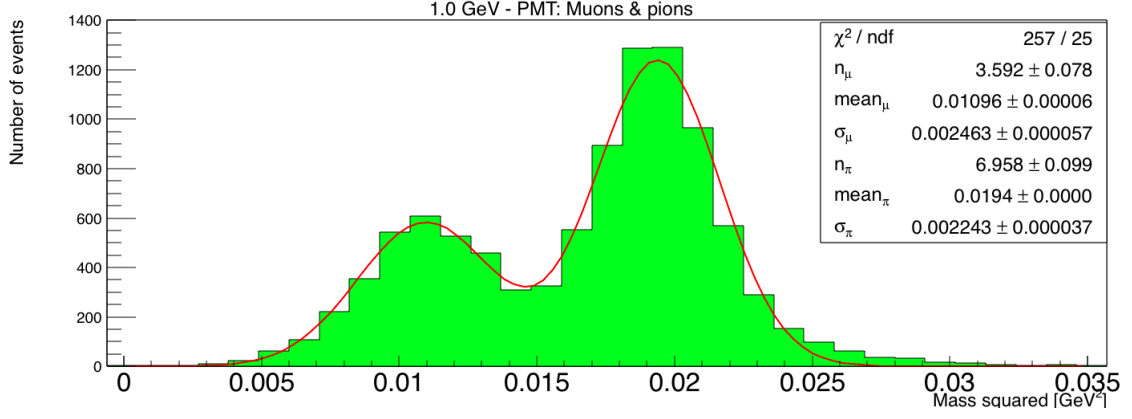
Figure 37: Number of events vs. mass squared of muons and pions at $p = 1.0$ GeV for the $|S_1 - S_2|$ configuration with corresponding Gaussian fits around their respective mean values of m^2.

Figure 38: Number of events vs. mass squared of protons at $p = 1.0$ GeV for the $|S_1 - S_2|$ configuration with corresponding Gaussian fit around mean value of m^2.

43

Figure 39: Number of events vs. mass squared of positrons at $p = 1.0$ GeV for the $|S_1 - S_3|$ configuration with corresponding Gaussian fit around mean value of m^2.

Figure 40: Number of events vs. mass squared of muons and pions at $p = 1.0$ GeV for the $|S_1 - S_3|$ configuration with corresponding Gaussian fits around their respective mean values of m^2.
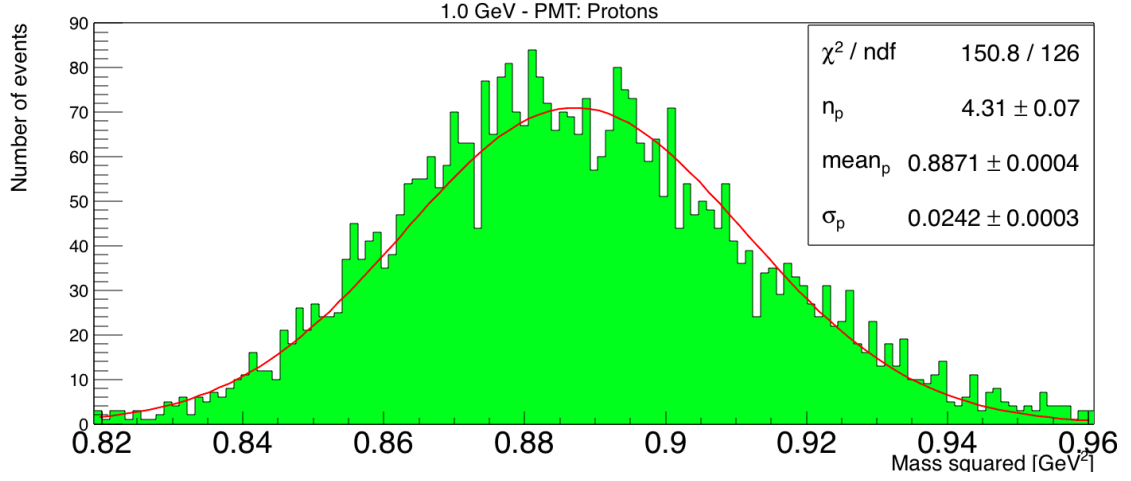
44

Figure 41: Number of events vs. mass squared of protons at $p = 1.0$ GeV for the $|S_1 - S_3|$ configuration with corresponding Gaussian fit around mean value of m^2.
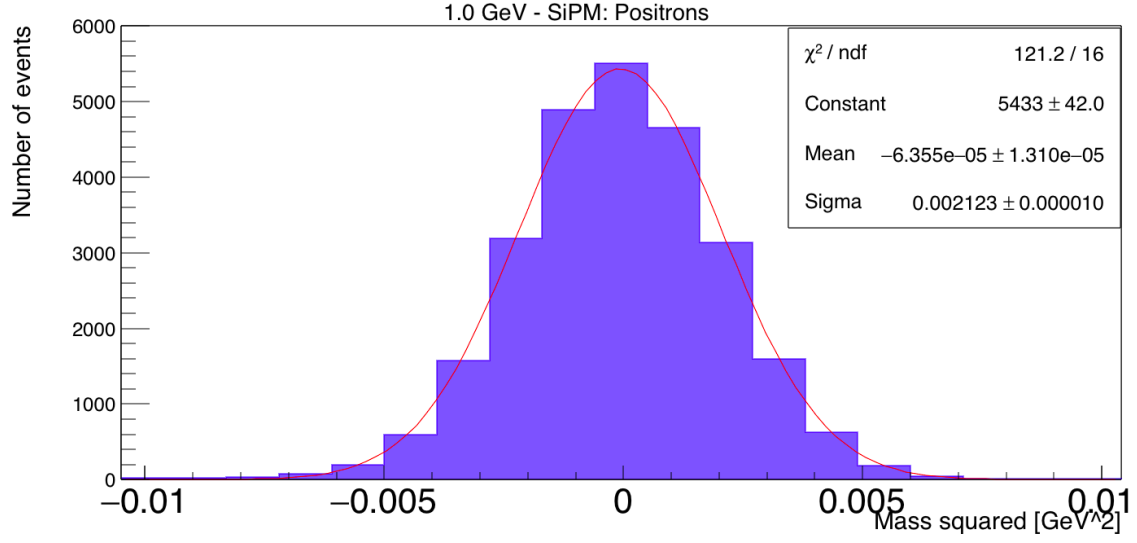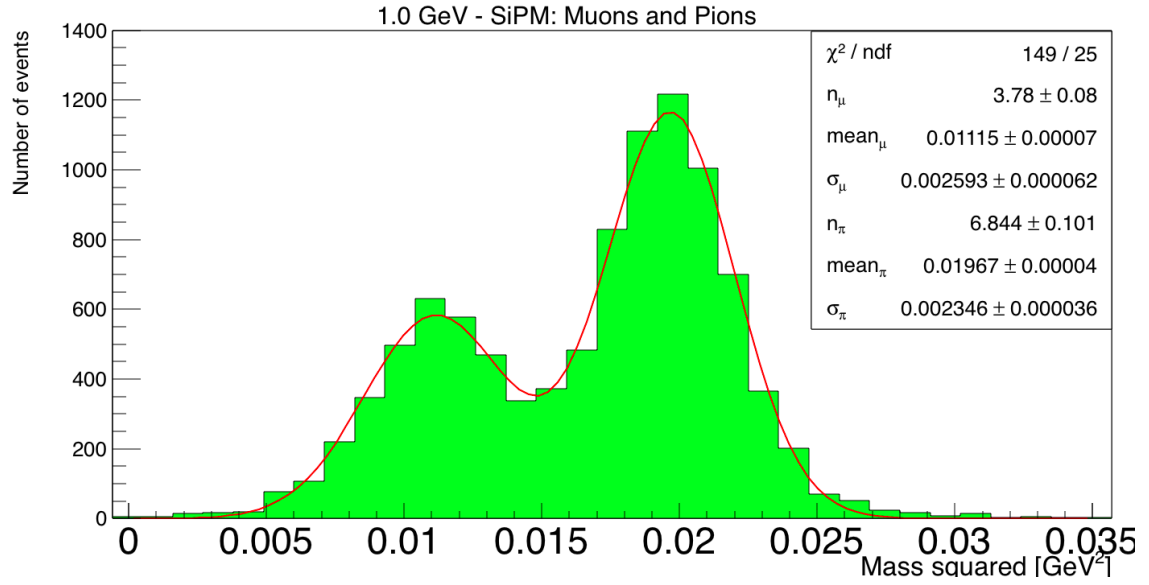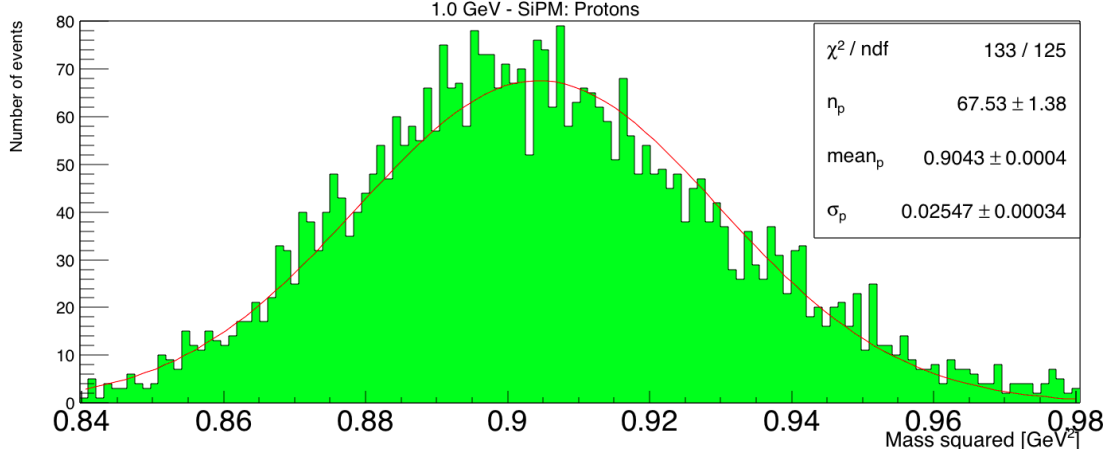
A summary of the figures is found in the table (5) below, i.e. the experimental and theoretical values of the mass squared for the two configurations as well as their respective uncertainties.

| Particles species | $S_1 - S_2$ | | $S_1 - S_3$ | | True |
	m^2_{exp} [GeV^2]	σ_{m^2} [GeV^2]	m^2_{exp} [GeV^2]	σ_{m^2} [GeV^2]	m^2_{th} [GeV^2]
e	-	$2.0 \cdot 10^{-3}$	-	$2.1 \cdot 10^{-3}$	$2.61 \cdot 10^{-7}$
μ	$1.10 \cdot 10^{-2}$	$2.5 \cdot 10^{-3}$	$1.12 \cdot 10^{-2}$	$2.6 \cdot 10^{-3}$	$1.12 \cdot 10^{-2}$
π	$1.94 \cdot 10^{-2}$	$2.2 \cdot 10^{-3}$	$1.97 \cdot 10^{-2}$	$2.3 \cdot 10^{-3}$	$1.96 \cdot 10^{-2}$
p	$8.87 \cdot 10^{-1}$	$2.4 \cdot 10^{-2}$	$9.04 \cdot 10^{-1}$	$2.5 \cdot 10^{-2}$	$8.80 \cdot 10^{-1}$

Table 6: Experimental values and their corresponding uncertainties of the mass squared of the $|S_1 - S_2|$ and $|S_1 - S_3|$ configurations for positrons, muons, pions and protons as well as the true values of their masses squared.

First comment to make concerns the mass squared of the positrons. Since their true mass squared is much smaller than the experimental resolution it is worthless to try to extract the positron mass, thus no experimental value is shown in table 6 for m^2_e. Concerning the other particle species (μ, π and p), it can be concluded that the experimental values for their mean masses squared for the two configurations are accurate since their true values fall within the given uncertainty. The precision of the values of m^2 is rather good too.

5.3 Identifying the uncertainty in momentum

In this section the uncertainty in momentum is identified for each of the particle species (e, μ, π and p). This is done by using the uncertainty in the timing measurement of the positrons $\left(\frac{\sigma_t}{t}\right)_e$, since they have no uncertainty in momentum, as the uncertainty in time for all the particle species. The uncertainty in momentum $(\frac{\sigma_p}{p})$ is then found for each species by inserting $\left(\frac{\sigma_t}{t}\right)_e$ from tables 4 and 5 and the values of $\sigma_{m^2_i}$ and $m^2_i, i \in \{e, \mu, \pi, p\}$ from table 6 in equation 5. The following values for $\frac{\sigma_p}{p}$ are found in the table below (7) for configurations $|S_1 - S_2|$ and $|S_1 - S_3|$. In order to make some conclusions on the different contributions to the uncertainty in the mass squared, $m^2 \frac{\sigma_p}{p}$ and $E^2 \frac{\sigma_t}{t}$ are also noted in the table below (see equation 5).

Particles species	$S_1 - S_2$			$S_1 - S_3$		
	σ_p/p	$m^2(\sigma_p/p)$ [GeV^2]	$E^2(\sigma_t/t)$ [GeV^2]	σ_p/p	$m^2(\sigma_p/p)$ [GeV^2]	$E^2(\sigma_t/t)$ [GeV^2]
e	$-$	$-$	$1.0 \cdot 10^{-3}$	$-$	$-$	$1.1 \cdot 10^{-3}$
μ	$6.1 \cdot 10^{-2}$	$6.9 \cdot 10^{-4}$	$1.0 \cdot 10^{-3}$	$6.4 \cdot 10^{-2}$	$7.1 \cdot 10^{-4}$	$1.1 \cdot 10^{-3}$
π	$1.6 \cdot 10^{-2}$	$3.2 \cdot 10^{-4}$	$1.1 \cdot 10^{-3}$	$1.8 \cdot 10^{-2}$	$3.5 \cdot 10^{-4}$	$1.1 \cdot 10^{-3}$
p	$1.3 \cdot 10^{-2}$	$1.2 \cdot 10^{-2}$	$1.9 \cdot 10^{-3}$	$1.4 \cdot 10^{-2}$	$1.2 \cdot 10^{-2}$	$2.0 \cdot 10^{-3}$

Table 7: Fractional uncertainty of the momentum, $m^2(\sigma_p/p)$ and $E^2(\sigma_t/t)$ for e, μ, π and p for the $S_1 - S_2$ and $S_1 - S_3$ configurations.

A first remark to make concerns the quantities: $m^2(\sigma_p/p)$ and $E^2(\sigma_t/t)$. They are included in the table 7 above because from equation 5 is can be found that: $\sigma_{m^2} \propto [m^2(\sigma_p/p) + E^2(\sigma_t/t)]$. Hence conclusions for each individual particle species on which of the uncertainties in either the spread in momentum or in the timing contributes the most to the identification in the mass of the particle in question can be made. This will now be discussed for each individual particle species.

Starting with the positrons, as they are considered ultra-relativistic particles and so by definition their momentum uncertainties do not affect the time-of-flight in any measurable way, the terms σ_p/p and $m^2(\sigma_p/p)$ are irrelevant. One can recall from section 5.1 that the uncertainty in the timing of the positrons was used as the uncertainty in timing for all the particles species. Therefore the largest contribution in the uncertainty of the determination of the mass squared of positrons is the uncertainty in the timing measurements. This holds for both configurations (i.e. S_1/S_2 and S_1/S_3).

Continuing with the muons, firstly regarding the uncertainty in the momentum (σ_p/p), it is higher as compared to the one of pions and protons (this concerns both configurations). As discussed in section 5.1, this is due to the fact that muons arise is the beam as a result of the decay of pions which leads to an additional spread in momentum. Comparing the configurations between themselves, one sees that the fractional uncertainty in momentum is slightly higher for the S_1/S_3 configuration as compared to the S_1/S_2 one. This is likely to be due to the larger distance from S_1 to S_3 relative to, S_1 to S_2. As more pions are able to decay and so more muons with different values of momentum would appear. Hence the same pattern follows through for the $m^2(\sigma_p/p)$ term. Concerning the timing uncertainty, S_1/S_3 has a slightly higher uncertainty than S_1/S_2. In general, for both configurations, the highest source of uncertainty in determination of the mass squared for muons resides in the timing measurements.

As for the pions, a lower relative uncertainty in momentum (as compared to muons) is observed for both configurations, as expected. Similarly here the uncertainties in the quantities proportional to the relative momentum are slightly higher for S_1/S_3 as compared to S_1/S_2, because of the same reasons as discussed in the previous paragraph.

Lastly, concerning the protons, they possess the lowest value of fractional uncertainty in momentum, however the highest $m^2(\sigma_p/p)$ as compared to the other particle species. This is due to the m^2 term, which is the highest for the protons as they have the highest mass among the studied particles species. The same applies for the $E^2(\sigma_t/t)$ term, again due to the high mass term which is included in E^2. As opposed to the other three particle species, the highest contribution to the uncertainty in the mass squared is from the uncertainty in the spread in momenta, as $m_p^2(\sigma_p/p) > E_p^2(\sigma_t/t)$.

In conclusion, positrons should be used to identify the uncertainty in the timing, with which their mass squared can also be identified. The m^2 of the muons and pions can also be determined, knowing that the highest source of uncertainty resides in the timing measurements. Hence to improve their identification the precision of the timing measurements would need to be enhanced. As for the protons, the highest source of uncertainty resides in their spread of momenta. Therefore, in order

to improve their identification the beam quality should rather be enhanced.

6   Summary

In this section a brief summary will be made for each sub-section, highlighting (if applicable) their findings, analysis and importance.

Starting with section 3, the time of flights of the particles were linked to their respective masses (in section 3.1), were it was found that a long time of flight corresponded to a heavy mass. A formula linking the two was derived (equation 1 in section 3.1 and full derivation in the appendix 8.2). A quantity named the predicted time delay was defined which would come to use when comparing theoretical and experimental times of flight. Tables 2 and 3 were made for the $|S_1 - S_2|$ and the $|S_1 - S_3|$ configurations respectively where the theoretical times of flight of the particles where calculated through the help of equation 2 and their corresponding predicted time delays identified. It was concluded that a higher mass particle had a longer time of flight for a given distance. Finally an equation linking the uncertainty in the mass squared with that of the time and the momentum was derived (equation 5).

The analysis was reported in section 4, where firstly distributions of the amplitude vs. time of flight were shown for the corresponding particles (section 4.1). The experimental predicted time delay was identified and was compared to the theoretical one, where a high precision was found. Due to the electronics of the SiPM readout for the $|S_1 - S_3|$ configuration, a correction due to a so-called *time-walk* effect was needed for its analysis. Such a correction was made successfully (section 4.2). In section 4.3, histograms of the number of events vs. mass squared of the individual particles were produced for the $|S_1 - S_2|$ and $|S_1 - S_3|$ configurations. Conclusions on the identification of the particles depending on the value of momenta were made, where in general they could be distinguished and identified. Further on in section 4.3.3 the different particles could yet again be identified, using a higher beam momentum, and this time also kaons were present. Lastly in section 4.3.4, positive and negative beams for a given momenta were compared. The general conclusion was that very few anti-protons were produced. Overall the histograms of section 4.3 followed well the information of the fraction of a given particle species in the beam for a certain value of momentum.

Lastly the uncertainty of the time of flight and mass squared of the particles was identified in sections 5.1 and 5.2 respectively by doing Gaussian fits of the histograms. Finally the uncertainty in momentum could hence be identified in section 5.3. All this information could be gathered together to provide useful information on how to more perform particle identification for each of the identified particle sprecies more precisely.

7 Conclusion

The interest of the project was to characterize and study the timing technique of a Time-of-Flight detector suggested for the upgrade of the ND280-T2K in Japan and as a timing detector for the SHiP experiment at CERN SPS. This was done through analysis of data taken in the summer of 2018 and acquired at the East Area (T9 and T10) at CERN PS where a beam of particles (of momenta ranging from 0.3 GeV to 5.0 GeV) was shot through a ToF-setup. The project focussed on the identification of particles that arrive onto plastic scintillator counters, whose readout system was based either on photomultiplier detectors (PMTs) or silicon photomultiplier detectors (SiPMs).

The identification was done by linking the time of flight of the particles to their corresponding masses (squared). In order to do this, firstly graphs of the amplitude versus the time of flight for the $|S_1 - S_2|$ and $|S_1 - S_3|$ configurations were made. For the latter configuration, a correction due to time-walk was needed. Then a formula for mass squared could be derived from the time of flight to be able to reconstruct the masses of the particles in the beam. This was done with success for all the particles. Lastly, the uncertainties of the time of flight, mass squared and momentum could be discussed and the most important one identified for each particle species. It was found that to improve PID of positrons, muons and pions, the precision in the timing measurements should be ameliorated and to improve the PID of the protons, the precision in the spread of momentum should be ameliorated. The latter would be done by upgrading the quality of the beam. In conclusion the goals of the project (to analyze the timing of the counters and identify the particles in the beam) were achieved.

8   Appendix

8.1   Derivation of equation (1)

We will here derive the equation (1), relating the square of the mass to the time difference. We start with the energy-momentum relation, which relates the total energy of a body in motion (E) with its rest mass (m) and its momentum (p). In SI units:

$$E^2 = m^2 c^4 + p^2 c^2 \Leftrightarrow m^2 c^4 = E^2 - p^2 c^2$$

Knowing that: $p = mv$ and $E = mc^2 \Rightarrow E = \frac{pc^2}{v}$, we obtain:

$$m^2 c^4 = \frac{p^2 c^4}{v^2} - p^2 c^2$$

$$\Leftrightarrow m^2 = \frac{p^2}{v^2} - \frac{p^2}{c^2} = \frac{p^2}{c^2}\left(\frac{c^2}{v^2} - 1\right)$$

$$\Leftrightarrow m^2 = \frac{p^2}{c^2}\left(\frac{c^2 t^2}{l^2} - 1\right)$$

From which we find equation (1):

$$\frac{m^2}{p^2} = \left(\frac{c\Delta t}{L}\right)^2 - 1$$

8.2 Derivation of uncertainty treatment of time and mass

Taking the total derivative of equation 3 one finds:

$$\delta_{m^2} = 2p\delta_p\left(\frac{t^2}{L^2} - 1\right) + 2t\delta_t\left(\frac{p^2}{L^2}\right) - \frac{2}{L^3}\delta_L(p^2t^2) \tag{8}$$

Using: $m^2 + p^2 = \frac{p^2t^2}{L^2} = E^2$, one can rewrite the following expressions:

$$\begin{cases} \frac{t^2}{L^2} - 1 = \frac{m^2}{p^2} \\ \frac{p^2}{L^2} = \frac{E^2}{t^2} \\ \frac{p^2t^2}{L^3} = \frac{E^2}{L} \end{cases}$$

Such that equation 8 becomes:

$$\delta_{m^2} = 2m^2\frac{\delta_p}{p} + 2E^2\frac{\delta_t}{t} - 2E^2\frac{\delta_L}{L} \tag{9}$$

Squaring both sides of equation 9, using: $\delta_i\delta_j = 0$ for $i, j \in \{p, t, L\}$, since they are independent of one another and finally changing the notation: $\delta \equiv \sigma$, one obtains for equation 9:

$$\sigma_{m^2} = \left[4m^4\left(\frac{\sigma_p}{p}\right)^2 + 4E^4\left(\frac{\sigma_t}{t}\right)^2 + 4E^4\left(\frac{\sigma_L}{L}\right)^2\right]^{\frac{1}{2}}$$

$$= 2[m^4\left(\frac{\sigma_p}{p}\right)^2 + E^4\left(\left(\frac{\sigma_t}{t}\right)^2 + \left(\frac{\sigma_L}{L}\right)^2\right)]^{\frac{1}{2}}$$

In general, $\frac{\sigma_L}{L} << \frac{\sigma_p}{p}, \frac{\sigma_t}{t}$, and so the uncertainty of the mass squared will be given by:

$$\sigma_{m^2} = 2\left[m^4\left(\frac{\sigma_p}{p}\right)^2 + E^4\left(\frac{\sigma_t}{t}\right)^2\right]^{\frac{1}{2}} \tag{10}$$

8.3 Calculation of the kaon decay length with time dilation

In this sub-section the decay length of kaons at momentum of $p = 1$ GeV and $p = 5$ GeV will be derived taking into account time dilation. The decay length is the distance a particle will travel before decaying. It is given by the following formula:

$$L = \beta c \tau = v \tau$$

With $\beta = v/c$ and τ the average life-time of the particle in question, in the reference frame of the particle, hence the *proper* life-time. If the speed of the particle is close to that of light, time dilation should be taken into account and the average life-time measured by an observer would be given by: $t' = \gamma \tau$, with γ, known as the Lorentz factor, given by: $\gamma = \frac{1}{\sqrt{1 - \frac{v^2}{c^2}}}$. Therefore the decay length observed by a *non-proper* reference frame is given by:

$$L' = \beta c t' = v t' = \gamma v \tau = \gamma L$$

The decay length of the kaon in its frame of reference (i.e. kaon at rest) is: $L = 3.711$ m. In order to find the decay length that would be observed by an observer (i.e. in the laboratory), knowledge of γ is necessary. In the following, γ will be found. For this, the velocity (v) of the kaon has to be determined. Once v is known, γ can be deduced. To find v, one makes use of the equation of relativistic momentum and the Lorentz factor (both in natural units, i.e. $[v] = [c] = 1$):

$$p = \gamma m v \text{ and } \gamma = \frac{1}{\sqrt{1 - v^2}}$$

Squaring both sides of the equation of relativistic momentum and replacing the Lorentz factor by its expression in terms of v one obtains:

$$p^2 = \frac{m^2 v^2}{1 - v^2} \Leftrightarrow \frac{p^2}{m^2} = \frac{v^2}{1 - v^2} \Leftrightarrow \frac{p^2}{m^2} - \frac{p^2}{m^2} v^2 = v^2 \Leftrightarrow v^2 \left(\sqrt{1 + \frac{p^2}{m^2}} \right) = \frac{p^2}{m^2}$$

Thus the speed is given by:

$$v = \frac{p/m}{1 + \frac{p^2}{m^2}}$$

Using known values for m_K and m_K^2 from section 3.1 the following velocities, Lorentz factors and dilated decay lengths for kaons of momentum: $p = 0$ GeV (i.e. at rest), $p = 1$ GeV and $p = 5$ GeV can be obtained and are shown in the table below:

p [GeV]	v [c]	γ	L' [m]
0	0	1	3.71
1	0.897	2.26	8.39
5	0.995	10.0	37.1

Table 8

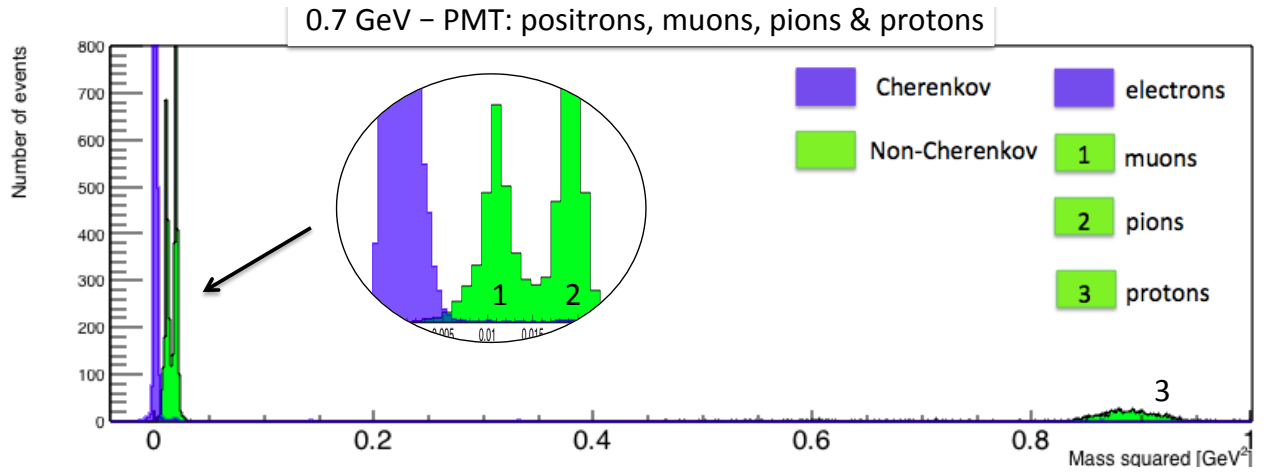## 8.4 Mass graphs $|S_1 - S_2|$ configuration

Figure 42: Number of events vs. m^2 calculated from $t_{S_2} - t_{S_1}$ at $p = 0.7$ GeV.
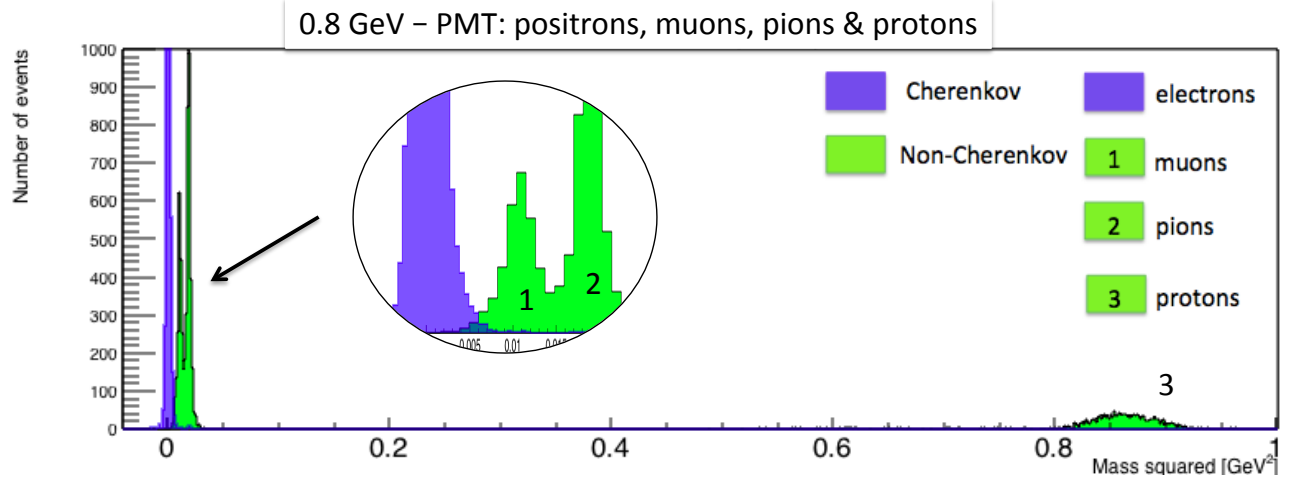

Figure 43: Number of events vs. m^2 calculated from $t_{S_2} - t_{S_1}$ at $p = 0.8$ GeV.
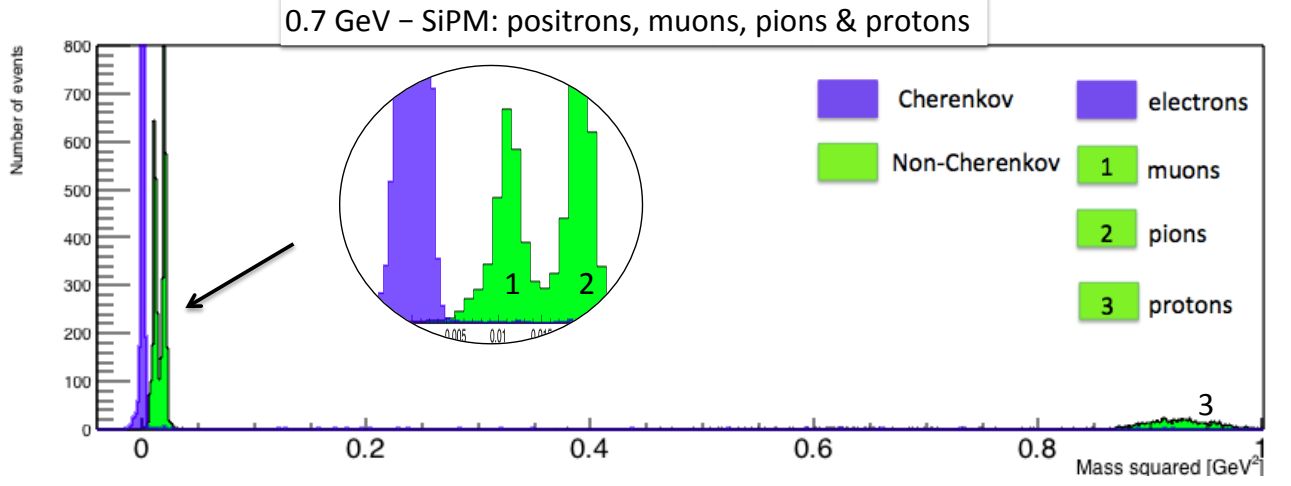
8.5   Mass graphs $|S_1 - S_3|$ configuration

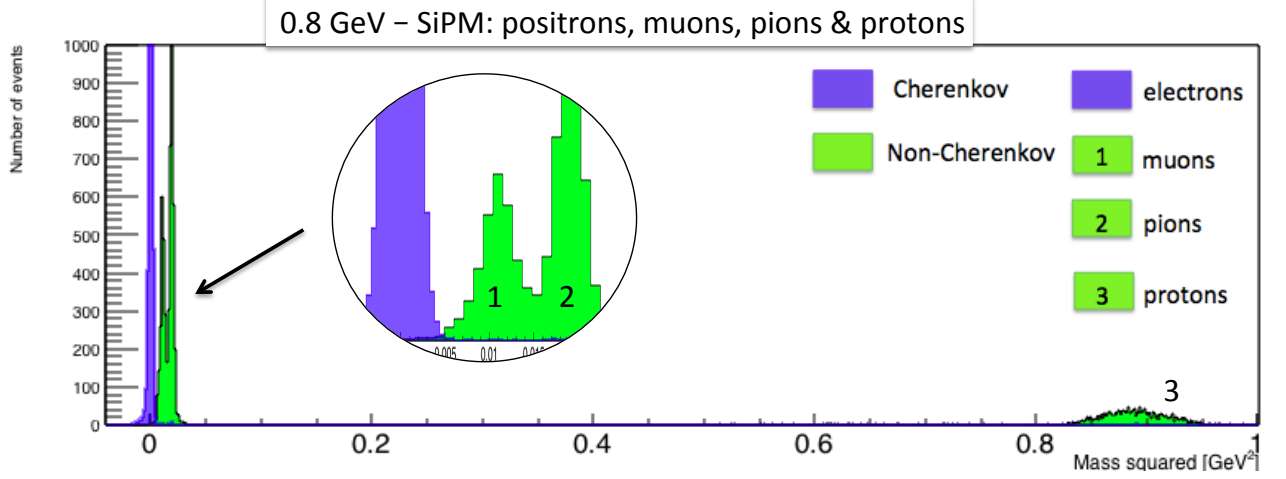Figure 44: Number of events vs. m^2 calculated from $t_{S_3} - t_{S_1}$ at $p = 0.7$ GeV.

Figure 45: Number of events vs. m^2 calculated from $t_{S_3} - t_{S_1}$ at $p = 0.8$ GeV.

References

[1] "T2K Experiment." http://t2k-experiment.org/t2k/physics-goals/.

[2] A. Korzenev, C. Betancourt, A. Blondel, D. Breton, A. Datwyler, D. Gascon, S. Gomez, M. Khabibullin, Y. Kudenko, J. Maalmi, P. Mermod, E. Noah, N. Serra, D. Sgalaberna, and B. Storaci, "Plastic scintillator detector with the readout based on an array of large-area SiPMs for the ND280/T2K upgrade and SHiP experiments," 2019. arXiv:1901.07785v1.

[3] T2K, Collaboration, K. Abe, (Kamioka., Observ.), and al.), "T2K ND280 Upgrade - Technical Design Report." arxiv:1901.03750, Jan 11, 2019.

[4] "SHiP Experiment." https://ship.web.cern.ch/ship/.

[5] Courtesy of Lau Gatignon (PS Team, CERN).

[6] "North Target." http://sba.web.cern.ch/sba/targets/TargetNorth.html.

[7] "Wikipedia - Photomultiplier." https://en.wikipedia.org/wiki/Photomultiplier.

[8] C. Betancourt *et al.*, "Application of large area SiPMs for the readout of a plastic scintillator based timing detector," *JINST* **12** no. 11, (2017) P11023, arXiv:1709.08972 [physics.ins-det].

[9] S. Gundacker, E. Auffray, N. Di Vara, B. Frisch, H. Hillemanns, P. Jarron, B. Lang, T. Meyer, S. Mosquera-Vazquez, E. Vauthey, and P. Lecoq, "SiPM time resolution: From single photon to saturation," *Nuclear Instruments and Methods in Physics Research Section A: Accelerators, Spectrometers, Detectors and Associated Equipment* **718** no. 1, (1 August 2018) 569–572.

[10] "Eljen Technology - Scintillators." https://eljentechnology.com/products/plastic-scintillators/ej-228-ej-230.

[11] A. Blondel, D. Breton, A. Dubreuil, A. Khotyantsev, A. Korzenev, J. Maalmi, A. Mefodev, P. Mermod, and E. Noah, "Study of timing characteristics of a 3 m long plastic scintillator counter using waveform digitizers," *Nuclear Instruments and Methods in Physics Research Section A: Accelerators, Spectrometers, Detectors and Associated Equipment* **877** no. 3, (2018) 9–15. arXiv:1610.05667v2.

[12] D. Breton, E. Delagnes, J. Maalmi, and P. Rusquart, "The WaveCatcher Family of SCA-Based 12-Bit 3.2-GS/s Fast Digitizers," May 2014. http://hal.in2p3.fr/in2p3-00995691. RT2014 - 19th Real-Time Conference, Nara, Japan.

[13] "Wikipedia - Constant fraction discriminator." https://en.wikipedia.org/wiki/Constant_fraction_discriminator.

[14] S. Gòmez, D. Gascon, G. Fernandez, A. Sanuy, J. Mauricio, R. Graciani Diaz, and D. Sanchez, "MUSIC: An 8 channel readout ASIC for SiPM arrays," April, 2016. Conference: SPIE Photonics Europe.